

Mixture of Multicenter Experts in Multimodal Generative AI for Advanced Radiotherapy Target Delineation

Yujin Oh^{1*}, Sangjoon Park^{2,3*}, Xiang Li^{1*}, Wang Yi⁴, Jonathan Paly⁴, Jason Efstathiou⁴, Annie Chan⁴, Jun Won Kim⁵, Hwa Kyung Byun⁶, Ik Jae Lee², Jaeho Cho², Chan Woo Wee², Peng Shu⁷, Peilong Wang⁸, Nathan Yu⁸, Jason Holmes⁸, Jong Chul Ye⁹, Quanzheng Li¹, Wei Liu^{8†}, Woong Sub Koom^{2†}, Jin Sung Kim^{2,10†}, and Kyungsang Kim^{1†}

¹*Center for Advanced Medical Computing and Analysis, Department of Radiology, Massachusetts General Hospital and Harvard Medical School, Boston, MA, USA*

²*Department of Radiation Oncology, Yonsei University College of Medicine, Seoul, South Korea*

³*Institute for Innovation in Digital Healthcare, Yonsei University, Seoul, South Korea*

⁴*Department of Radiation Oncology, Massachusetts General Hospital, Boston, MA, USA*

⁵*Department of Radiation Oncology, Gangnam Severance Hospital, Seoul, South Korea*

⁶*Department of Radiation Oncology, Yongin Severance Hospital, Yongin, Gyeonggi-do, Korea*

⁷*School of Computing, University of Georgia, GA, USA*

⁸*Department of Radiation Oncology, Mayo Clinic, AZ, USA*

⁹*Kim Jaechul Graduate School of AI, Korea Advanced Institute of Science and Technology, Daejeon, South Korea*

**These authors contributed equally: Yujin Oh, Sangjoon Park, and Xiang Li*

†Correspondence to Wei Liu (liu.wei@mayo.edu), Woong Sub Koom (mdgold@yuhs.ac), Jin Sung Kim (jinsung@yuhs.ac) or Kyungsang Kim (kkim24@mgh.harvard.edu)

Abstract

Clinical experts employ diverse philosophies and strategies in patient care, influenced by regional patient populations. However, existing medical artificial intelligence (AI) models are often trained on data distributions that disproportionately reflect highly prevalent patterns, reinforcing biases and overlooking the diverse expertise of clinicians. To overcome this limitation, we introduce the Mixture of Multicenter Experts (MoME) approach. This method strategically integrates specialized expertise from diverse clinical strategies, enhancing the AI model's ability to generalize and adapt across multiple medical centers. The MoME-based multimodal target volume delineation model, trained with few-shot samples including images and clinical notes from each medical center, outperformed baseline methods in prostate cancer radiotherapy target delineation. The advantages of MoME were most pronounced when data characteristics varied across centers or when data availability was limited, demonstrating its potential for broader clinical applications. Therefore, the MoME framework enables the deployment of AI-based target volume delineation models in resource-constrained medical facilities by adapting to specific preferences of each medical center only using a few sample data, without the need for data sharing between institutions. Expanding the number of multicenter experts within the MoME framework will significantly enhance the generalizability, while also improving the usability and adaptability of clinical AI applications in the field of precision radiation oncology.

Introduction

The integration of artificial intelligence (AI) into clinical practice is increasingly recognized for its potential to enhance patient care, particularly in fields where precision is critical, such as radiation oncology^{1,2}. AI has shown promise in automating and improving critical aspects of radiation therapy, such as target volume contouring and treatment planning, including determining the scope and dose of treatment from a patient's planning computed tomography (CT) scan³⁻⁵. However, a significant challenge remains: ensuring the generalizability of AI models across diverse institutional healthcare settings. As shown in Fig. 1(a), variations across centers, such as differences in regional populations, imaging modalities, and clinical protocols, contribute to the difficulty of applying pre-trained AI models developed in one context to distinct data distributions in others.

Recent advancements have begun to tackle this challenge by incorporating multimodal data considerations into AI models. In radiation therapy, target volume delineation requires more than just visual cues; factors such as patient's surgical history, pathology, and disease-specific biomarker levels are also essential. Multimodal AI models, which combine clinical context with imaging data, have demonstrated superior generalization capabilities across various datasets compared to their unimodal models. This is attributed to the crucial role of clinical text, typically presented in a structured format, in improving the generalizability of AI models across various types of datasets. Promising outcomes of multimodal models have been demonstrated across various cancer types^{4,5}. Moreover, the advancement of large language models (LLMs) in medicine⁶⁻⁸ has accelerated the development of multimodal AI, improving generalizability across different imaging modalities and institutional settings.

Despite these advancements, traditional AI models trained on data from a limited number of institutions continue to suffer from biases that reflect the characteristics of those specific settings. This bias hinders the adaptability of AI models to diverse clinical settings, resulting in suboptimal performance. Addressing this issue is especially critical, particularly in radiation therapy where substantial variability in target volume delineation practices exists, even with consensus guidelines⁹⁻¹¹. Prostate cancer radiotherapy is a prime example, as treatment strategies can vary considerably across institutions, driven by differences in regional patient populations and institutional protocols^{12,13}, as illustrated in Fig. 1(b). This variability complicates the implementation of AI-driven tools for target volume contouring, compared to the relatively broader acceptance of AI for contouring organs-at-risk (OAR)^{14,15}.

Addressing bias in medical AI models requires effective multicenter training strategies that can integrate diverse data sources while maintaining confidentiality, given the restricted scope of clinical data sharing. Federated learning offers a promising solution by decentralizing data storage and enabling collaboration across institutions^{16,17}. However, despite its potential, the widespread adoption of federated learning in practical applications remains limited due to several challenges. Its performance often falls short compared to centralized data training methods, and issues such as straggler problems can introduce instability in the training process. Moreover, federated learning is vulnerable to security threats, including data poisoning and inference attacks, which compromise model integrity. These limitations have constrained its widespread adoption. Recent advancements in the Mixture of Experts (MoE)¹⁸ training mechanism have transformed the adaptation of AI models to diverse data distributions within continual learning frameworks. This approach significantly enhances the robustness and adaptability when confronted with previously unseen data patterns¹⁹⁻²¹. Building upon these advances, we propose a Mixture of Multicenter Experts (MoME) as a novel multimodal AI training approach to address biased inference and enable AI models to better reflect the needs of individual institutions. The MoME can not only mitigate data bias but also improve the generalizability and adaptability of medical AI, expanding its applicability across diverse clinical settings.

The proposed MoME framework integrates a shared path with center-specific router paths, enabling the model to adapt to diverse data distributions and clinical settings with minimal data input. As illustrated in Fig. 1(b), this design allows the model to efficiently adapt to each medical center data distribution with only 10 to 20 samples per center using the router to finetune the best pre-trained model in the MoME framework. This is a significant improvement over traditional training methods, which often require hundreds or even thousands of labeled datasets to mitigate model bias to dominant institution’s data distribution. This adaptability ensures that the model can account for the unique treatment approaches and delineation strategies of each institution, resulting in more personalized and precise treatment planning. Moreover, the MoME framework supports flexible and dynamic inference scenarios across diverse clinical settings. During deployment, the model can quickly adjust to local practices and patient populations by using a few sample test datasets from a new center to select the most suitable center-specific router path. Crucially, the scalability of the MoME framework is enhanced by its distributed model weights¹, facilitating integration across multiple institutions globally and allowing for the selection of the most relevant inference scenarios tailored to their practices. Moreover, the straightforward MoME framework can be utilized as a plug-in module for diverse medical AI frameworks, facilitating efficient knowledge

¹<https://github.com/tvseg/MoME-RO>

sharing between medical centers while allowing for continuous improvement as new data from diverse sources is efficiently incorporated.

In this study, we applied MoME to address the limitations of current AI models in prostate cancer target volume delineation, that exhibits significant variability across institutions. Furthermore, we extend our approach to MoME fine-tuning by incorporating in-house fine-tuning for hospitals with restricted data sharing to address clinical deployment challenges when adapting AI models to new data distributions. Our results demonstrate that a MoME-based model not only significantly outperforms traditional AI models in target volume contouring, but also aligns its overall distribution more closely with that of each institution. This improvement is especially pronounced in cases with diverse data characteristics, highlighting the potential of the MoME approach to advance the adoption of AI in radiation oncology while addressing the challenges posed by subtle differences in institutional treatment protocols and patient distributions across each site.

Results

Center-specific radiotherapy target delineation strategy We collected prostate cancer datasets from five centers and analyzed their distinct characteristics and target delineation tendencies, as illustrated in Fig. 1(a). Centers A (Yonsei Cancer Center; YCC) and B (Yongin Severance; YS), both in South Korea, exhibit similar treatment protocols and image acquisition settings. Although Center B has a different National Comprehensive Cancer Network (NCCN)²² risk group distribution compared to Center A, their treatment strategies remain largely similar, resulting in relatively homogeneous datasets. Center C (Gangnam Severance; GS), also based in South Korea, differs more from Centers A and B in terms of image acquisition settings, NCCN risk group distribution, and treatment strategies, although the racial distribution of patients is consistent. In contrast, Centers D (Massachusetts General Hospital; MGH) and E (MAYO Clinic) in the US show greater variability, with substantial differences in national healthcare systems, NCCN risk group distribution, and treatment strategies. This increasing divergence across centers introduces significant challenges for model generalization, particularly when both imaging environments and clinical strategies differ substantially. These findings emphasize the need for adaptive approaches, such as the Mixture of Multicenter Experts (MoME), which can robustly handle cross-center variability. A detailed summary of the data distribution is provided in Supplementary Table 1 and further discussed in the Methods section.

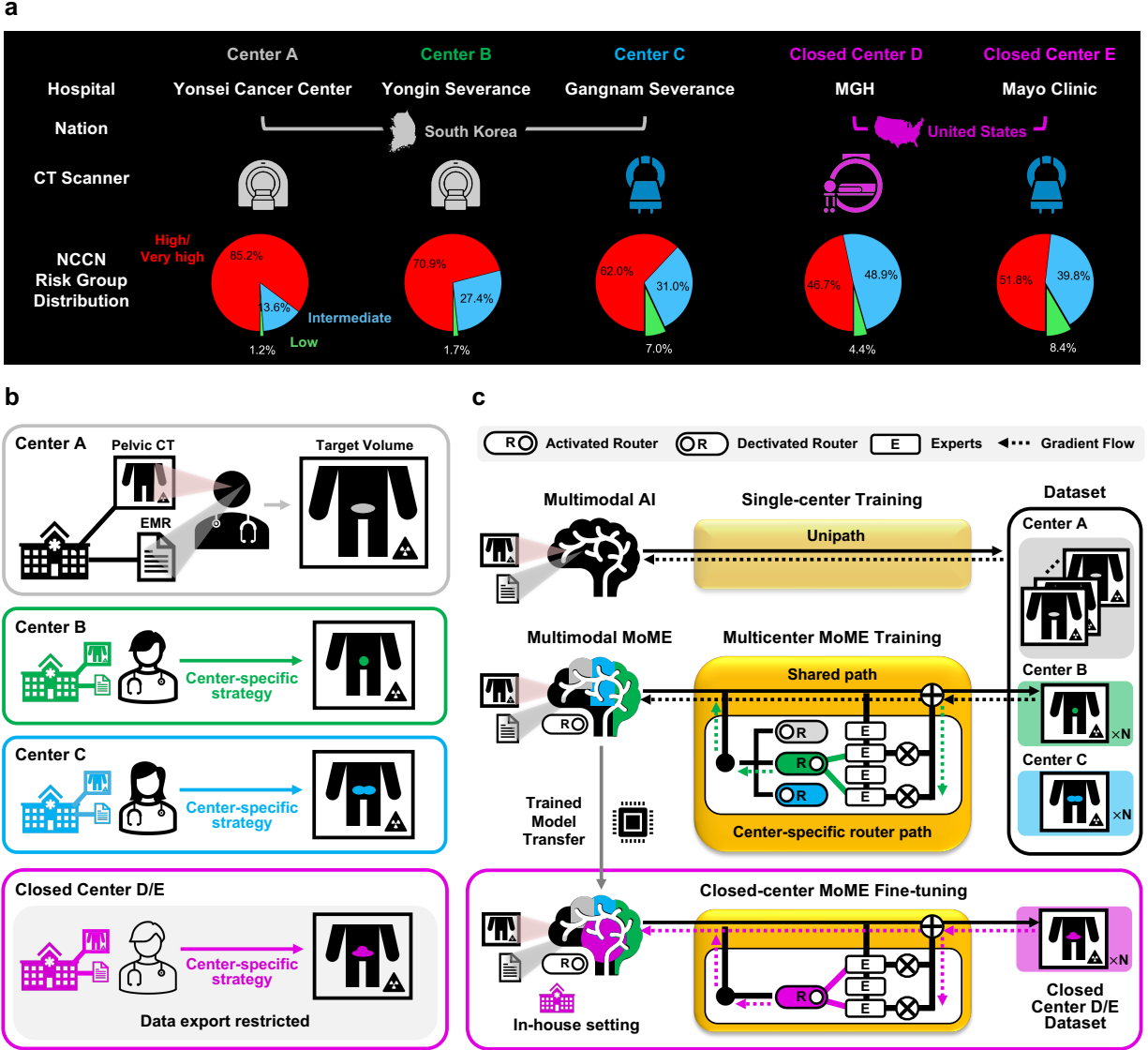


Figure 1: Schematic of multimodal-multicenter AI training using our proposed Mixture of Multicenter Experts (MoME) approach. (a) Characteristics of each center, which can influence their radiotherapy target delineation tendencies, emphasize the need for an adaptive AI training approach. (b) Radiotherapy target delineation strategies for prostate cancer patients vary slightly across various centers, which limits the generalizability of AI models. (c) Compared to traditional unipath single-center training, our MoME training leverages both shared and center-specific routing paths. These paths activate relevant expert modules customized to the unique characteristics of each center given a few-shot dataset. Moreover, where data export is restricted, a closed center MoME fine-tuning is employed, allowing for in-house model adaptation.

Analysis of model performance across centers We first trained baseline methods under the traditional single-center AI training setting (Table 1(a)). Models trained exclusively on data from Center

A exhibited overfitting to the training distribution, leading to suboptimal performance on Centers B and C datasets, which were not seen by the model during training under the single-center setting, yielding Dice scores of 0.670 and 0.520 for Centers B and C, respectively. However, incorporating both imaging and textual data, as described in our previous study ⁴, the multimodal approach improved performance on external datasets compared with vision-only models, with Dice scores of 0.732 and 0.597 for Centers B and C, respectively.

Then, we performed experiments under the newly introduced multicenter AI training setting (Table 1(b)), which utilizes few-shot datasets from Centers B and C in addition to the training data from Center A. Despite this, vision-only models showed only marginal improvement over the single-center training setting, with Dice scores of 0.680 and 0.561 for Centers B and C, respectively. In contrast, when trained with the vanilla multimodal AI, planning target volume (PTV) delineation performance significantly improved, particularly for Center C, showing 0.667 in Dice metric, where acquisition settings differed from those at Centers A and B. Moreover, when trained with our proposed MoME multimodal AI, PTV delineation performance improved further, demonstrating stable performance above 0.7 by achieving Dice scores of 0.747, 0.750, and 0.716 for Centers A, B, and C, respectively. For comparison, we re-trained a publicly available 3D text-driven multimodal segmentation framework, ConTEXTualNet ²³. ConTEXTualNet demonstrated comparable performance to vanilla multimodal AI training but still showed suboptimal performance for centers with few-shot datasets, with Dice scores of 0.721 and 0.663 for Centers B and C, respectively. The performance gap and statistical significance between vision-only and vanilla multimodal training methods compared to our proposed MoME training method for each center dataset are visualized in Fig. 2(a).

We performed a qualitative comparison of different approaches under the multicenter AI training setting to assess their clinical performance. As shown in Fig. 2(b), for an intermediate-risk, node-negative case, the institutional policy at Center C was to typically avoid prophylactic nodal irradiation. However, both the vision-only and the multimodal models mistakenly included nodal regions in the target. In contrast, the proposed multimodal MoME model accurately focused on the prostate while also providing margin settings that closely aligned with the institution’s guidelines. Further, as illustrated in Fig. 2(c), in another intermediate-risk, node-negative case, while all models correctly excluded elective nodal areas, significant differences were observed in the PTV margins. The institutional policy at Center C tends to define the PTV with a more generous margin around the gross tumor, a practice not reflected in the tighter margins predicted by the vision-only and the multimodal models. In contrast, the multimodal MoME model accurately

Table 1: PTV delineation performance for prostate cancer patients with MoME.

Dataset	Metric	(a) Single-center AI Training		(b) Multicenter AI Training			
		Vision-only AI ²⁴	Multimodal AI	Vision-only AI ²⁴	Multimodal AI		
			Vanilla ⁴		Vanilla ⁴	MoME (Ours)	ConTEXTualNet ²³
Center A (n=169 patients)	Dice ↑	0.727 (0.699-0.753)	0.736 (0.708-0.764)	0.717 (0.689-0.743)	0.755 (0.731-0.777)	0.747 (0.721-0.772)	0.744 (0.718-0.767)
	IoU ↑	0.598 (0.569-0.626)	0.610 (0.580-0.639)	0.586 (0.557-0.614)	0.629 (0.602-0.653)	0.623 (0.594-0.648)	0.617 (0.591-0.643)
	HD-95 ↓	3.338 (2.860-3.829)	3.690 (3.002-4.373)	3.319 (2.906-3.774)	3.032 (2.638-3.441)	3.407 (2.898-3.956)	3.409 (2.916-3.910)
Center B (n=117 patients)	Dice ↑	0.670 (0.639-0.700)	0.732 (0.708-0.756)	0.680 (0.650-0.709)	0.738 (0.714-0.762)	0.750 (0.725-0.773)	0.721 (0.697-0.744)
	IoU ↑	0.525 (0.492-0.557)	0.593 (0.567-0.620)	0.536 (0.503-0.567)	0.600 (0.574-0.628)	0.617 (0.588-0.643)	0.577 (0.551-0.602)
	HD-95 ↓	3.191 (2.981-3.395)	3.155 (2.815-3.599)	3.196 (2.984-3.400)	3.097 (2.839-3.356)	3.040 (2.773-3.294)	3.042 (2.775-3.313)
Center C (n=129 patients)	Dice ↑	0.520 (0.482-0.557)	0.597 (0.559-0.635)	0.561 (0.527-0.595)	0.667 (0.633-0.698)	0.716 (0.688-0.744)	0.663 (0.627-0.698)
	IoU ↑	0.380 (0.343-0.415)	0.458 (0.419-0.495)	0.415 (0.381-0.449)	0.530 (0.495-0.564)	0.582 (0.553-0.613)	0.526 (0.489-0.560)
	HD-95 ↓	5.384 (4.696-6.071)	6.402 (5.339-7.454)	5.417 (4.790-6.100)	4.101 (3.457-4.782)	4.132 (3.319-5.045)	5.817 (4.888-6.803)

predicted a broader PTV margin consistent with Center C’s practice, proving its ability to integrate institutional policies and more precisely delineate the target volume.

To systematically compare and quantify the impact of institutional practices on target delineation beyond individual examples, we introduced the GTV-to-PTV ratio (GPR), defined as the ratio of gross tumor volume (GTV) to PTV. This metric was proposed because it effectively captures two key factors where inter-institutional differences are likely to arise in prostate cancer radiotherapy: whether prophylactic nodal irradiation (PNI) is performed and the extent of margin applied to the gross tumor volume. When nodal irradiation is performed, the pelvic lymph nodes are included in the PTV, leading to a lower GPR (Fig. 2(d)). Furthermore, the margin applied around the gross tumor also influences the GPR, making it a comprehensive measure that reflects both these key aspects of radiotherapy practice. To compare each institution’s approach, we exclusively analyzed N0 patients, who have been pathologically diagnosed with no metastasis in the lymph nodes, and excluded N1 patients, whose treatment planning might overlap across institutions.

We first compared the GPR distributions of the ground truth labels, vision-only AI, vanilla multimodal AI, and MoME models on test data from centers A, B, and C (Figs. 2(e), (f), and (g), respectively). The results from the ground truth GPR distribution for each dataset highlighted two distinct peaks around GPR values of 20%, corresponding to cases with higher and lower GPR values, respectively. This provides a clear visualization of the differences in clinical practices between the centers. Specifically, for Centers A and B, a greater concentration of data was found in

the lower GPR range, indicating that PNI is routinely performed in a significant proportion of patients, even in intermediate-risk cases. In contrast, the ground truth GPR distribution for Center C displayed a higher distribution of GPR values, indicating a lower frequency of PNI, particularly for intermediate-risk patients. This illustrates a critical divergence in clinical practice patterns, where Centers A and B frequently employ PNI across very-high, high, and intermediate-risk groups. Meanwhile, Center C tends to exclude PNI, particularly for intermediate-risk patients, reflecting a more conservative approach in this cohort.

In the predicted GPR distributions across all datasets, the vision-only model consistently exhibited a high prevalence of low GPR values, indicating over-inclusion of regional nodes and a failure to capture the clinical context accurately. In contrast, both the vanilla multimodal and MoME models demonstrated GPR distributions closely aligned with the ground truth for Centers A and B, showing no significant differences in the internal validation setting, as well as in external validation settings with similar environments and practice patterns. However, in Center C, where acquisition settings and clinical practices differ, the MoME model showed a closer alignment with the original GPR distribution compared to the vanilla multimodal AI model, particularly where these variations were more pronounced. Overall, the MoME model consistently generated GPR values most closely matching the ground truth, demonstrating its ability to adapt to institution-specific practices and outperform both the vision-only and vanilla multimodal AI models in customizing target delineation.

When stratified by risk group, the vision-only model consistently exhibited a high concentration of low GPR values across all risk levels, further confirming its limitations in capturing crucial clinical subtleties. While the vanilla multimodal AI model showed some improvement, it still failed to accurately reflect the ground truth distribution. In contrast, the MoME model produced the most accurate GPR distribution, closely aligning with the original ground truth values across all risk groups (Supplementary Fig. 2). This highlights the MoME model's superior capacity not only to incorporate clinical context but also to adapt to institution-specific practices, resulting in more precise and context-aware target delineation.

Center-specific inference reflects radiotherapy planning strategy During inference, a key advantage of our MoME module is its ability to select a center-specific router tailored to each center's dataset characteristics. This capability allows us to analyze model predictions by choosing a corresponding or different router path. To evaluate the overall tendencies of each center-specific router, we first tested the entire test dataset from each center as input, activating the corresponding

center-specific routers. Specifically, we visualized the overall trends in how each router captures the center's unique target delineation strategy using violin plots of GPR values, enabling us to assess how target distribution shifts with the application of these center-specific routers.

For Center A, the GTV-to-PTV ratio (GPR) distribution aligned most closely with the center's original practice when using the Center A expert, characterized by frequent prophylactic nodal irradiation (PNI) and more generous margins, resulting in lower GPR values. The Center B expert also produced a GPR distribution that closely followed Center A's practice. In contrast, using the Center C expert shifted the GPR distribution toward higher values, indicating a lower proportion of nodal irradiation and the application of tighter margins, consistent with Center C's practice pattern. This trend was particularly evident in the intermediate/low-risk group, where clinical discretion plays a greater role compared to the high/very high-risk group, where PNI was more clearly indicated (Supplementary Fig. 3(a), (b)). Furthermore, even among the Center A and B experts, the Center A expert produced a GPR distribution that more closely matched the original ground truth across all risk groups.

Despite having the smallest proportion of high/very high-risk patients, Center B's GPR remained relatively low, reflecting treatment practices similar to those of Center A. When using the Center B expert, the GPR distribution closely aligned with Center B's original practice. In contrast, using the Center C expert led to an increase in GPR, indicating less frequent PNI and tighter PTV margins. Risk group analysis further demonstrated that the Center B expert produced the most consistent GPR values across all risk groups, closely matching the original GPR distribution (Supplementary Fig. 3(c), (d)). Although the Center B expert provided the closest match, the Center A expert also produced a GPR distribution more aligned with the ground truth than the Center C expert, suggesting that treatment protocols at Centers A and B are more similar to each other than to those of Center C.

Center C exhibited the most distinct pattern among the three centers. While the proportion of high/very high-risk patients was lower than at Center A, it exceeded that of Center B. In general, Center C demonstrated higher GPR values, reflecting its clinical practice of performing PNI less frequently and applying tighter PTV margins. When using the Center C expert, the GPR distribution aligned more closely with Center C's original clinical patterns compared to other expert routers, consistently yielding higher GPR values. This suggests a reduced frequency of PNI and the application of smaller PTV margins, a trend observed across all risk groups, including both high/very high-risk and low/intermediate-risk groups. Notably, even in the high/very high-risk

group, where PNI is typically performed, the GPR remained higher than the ground truth. This indicates that the Center C expert router may have overemphasized the institution’s practice of less frequent PNI, potentially reflecting an excessive alignment with Center C’s specific clinical tendencies (Supplementary Fig. 3(e), (f)).

To further analyze the working mechanism of the proposed MoME module, we visualized the intermediate processes within the center-specific router and its effects on expert module activation. During inference, the center-specific router automatically assigns the most appropriate expert layers for each input within our MoME module. To evaluate how this unique routing process contributes to the model’s adaptation to each center, we counted the number of times each expert was selected for every patch within the input and normalized these counts by the total number of patches. Then, we analyzed the frequency of each expert activation for every MoME modules in each network layer, designating the bottom-most layer as Layer #0 and the top-most layer as Layer #3.

Firstly, to visualize trends for each center dataset, we averaged the results across all patients for each center. As shown in Fig. 3(b), the frequency of activated top-k expert modules for each dataset by using the corresponding center-specific router was visualized, e.g., the Center A-specific router for the Center A dataset. The activation patterns revealed sparse and distinct expert usage across layers, with different experts being activated for each center-specific router path. These variations demonstrates how MoME’s expert activation adapts to the specific characteristics of each center, potentially enhancing performance across diverse data distributions. Next, we investigated the frequency of activated top-k expert modules for an identical input CT scan. As shown in Fig. 3(c), the activation patterns for each center-specific router exhibited frequency trends similar to those observed in Fig. 3(b), indicating the MoME module’s ability to adapt its center-specific activation, even when processing an individual patient’s CT scan from Center C. In qualitative analysis for this case, as shown in Fig. 3(d), different center-specific routers resulted in notable differences in the predicted outputs. Applying the Center A- and B-specific routers to the same input CT scan produced a result with a slightly enlarged PTV margin and included PNI compared to the ground truth PTV. In contrast, using the corresponding Center C-specific router yielded a prediction where the Prostate PTV closely aligned with the ground truth, featuring an appropriate PTV margin and no PNI. These results indicate that MoME’s center-specific router adaptively selects expert layers, optimizing the model predictions to each center’s characteristics and enhancing its generalizability across diverse data distributions.

Data efficient few-shot fine-tuning on closed center dataset To evaluate the proposed MoME training method in closed center settings, where data export is restricted, we conducted few-shot fine-tuning in-house. We adapted the pre-trained model to the newly introduced center dataset, leveraging the computing resources available within the center. To compare the training efficiency of each vision-only, vanilla multimodal, and MoME model, we monitored the performance of each method in PTV contouring as the size of the few-shot fine-tuning dataset progressively increased. Table 2 summarizes the performance of these methods across diverse closed center datasets.

For Center D, in the 0-shot inference setting, both vision-only and multimodal models showed suboptimal Dice scores of 0.384 and 0.410, respectively. In contrast, the MoME approach, which utilized the Center B-specific router due to its policy similarities with Center D, achieved a higher Dice score of 0.465 with Center B-specific inference. In the subsequent few-shot fine-tuning process starting from the pre-trained checkpoint, the performance gap between methods became more pronounced as the number of fine-tuning shots increased. With 1-shot, 2-shot, and 3-shot fine-tuning, the MoME model demonstrated superior performance, yielding Dice scores of 0.503, 0.558, and 0.582, respectively. Notably, the MoME model consistently outperformed both the vision-only and multimodal models across all fine-tuning settings. Fig. 4(a) further compares the performance of different methods for each fine-tuning shot.

For Center E, in the 0-shot inference setting as shown in Table 2, both vision-only and multimodal models exhibited limited effectiveness, with Dice scores of 0.327 and 0.476, respectively. In contrast, the MoME approach, when utilizing Center C-specific routers, achieved a higher Dice score of 0.558. This is notable because Center C shares the most similar data acquisition conditions with Center E, as detailed in Supplementary Table 1. Then, we further fine-tuned the network using Center E dataset. In the few-shot fine-tuning settings, the multimodal MoME consistently outperformed baseline models. Specifically, the MoME approach achieved Dice scores exceeding 0.6 across all datasets, with Dice scores of 0.630, 0.631, and 0.648 for the 1-shot, 2-shot, and 3-shot settings, respectively. The performance gains compared to vision-only and vanilla multimodal training mechanisms are also illustrated in Fig. 4(b). For both closed center fine-tuning experiments, our proposed MoME fine-tuning method demonstrated generalizability and adaptability for distinct radiotherapy delineation strategies.

We further analyzed the GPR distribution within the closed center setting (Fig. 4(c-d)). The ground truth GPR distribution, characterized by two peaks around 20%, served as the reference point. During zero-shot inference, the vision-only model consistently skewed towards lower GPR

Table 2: PTV delineation performance on closed center dataset with different size of few-shot fine-tuning dataset.

Method	Metric	Closed Center D (n=45 patients)					
		0-shot	1-shot	2-shots	3-shots		
Vision-only AI	Dice ↑	0.384 (0.320-0.448)	0.401 (0.334-0.468)	0.420 (0.360-0.476)	0.473 (0.433-0.513)		
	IoU ↑	0.263 (0.211-0.316)	0.279 (0.223-0.334)	0.288 (0.238-0.336)	0.321 (0.287-0.355)		
	HD-95 ↓	6.507 (5.577-7.511)	6.651 (5.712-7.646)	6.706 (5.760-7.762)	6.119 (5.197-7.170)		
Multimodal AI	Dice ↑	0.410 (0.368-0.452)	0.411 (0.359-0.464)	0.482 (0.430-0.533)	0.505 (0.451-0.556)		
	IoU ↑	0.273 (0.238-0.307)	0.276 (0.232-0.322)	0.335 (0.292-0.378)	0.358 (0.311-0.402)		
	HD-95 ↓	7.202 (6.117-8.315)	9.003 (7.498-10.521)	7.303 (5.944-8.724)	6.402 (5.162-7.685)		
Center-specific Inference							
		Center A	Center B	Center C			
Multimodal MoME	Dice ↑	0.444 (0.395-0.495)	0.465 (0.419-0.516)	0.423 (0.377-0.469)	0.503 (0.455-0.551)	0.558 (0.506-0.607)	0.582 (0.529-0.633)
	IoU ↑	0.302 (0.262-0.346)	0.318 (0.280-0.363)	0.281 (0.244-0.320)	0.353 (0.309-0.396)	0.407 (0.361-0.452)	0.433 (0.381-0.482)
	HD-95 ↓	7.978 (6.451-9.768)	9.152 (7.429-10.999)	10.056 (8.119-11.991)	8.272 (6.620-9.995)	6.853 (5.410-8.585)	5.327 (4.131-6.707)
Method	Metric	Closed Center E (n=73 patients)					
		0-shot	1-shot	2-shots	3-shots		
Vision-only AI	Dice ↑	0.327 (0.295-0.359)	0.500 (0.469-0.533)	0.510 (0.478-0.540)	0.476 (0.438-0.513)		
	IoU ↑	0.205 (0.180-0.232)	0.345 (0.315-0.374)	0.352 (0.324-0.379)	0.327 (0.293-0.360)		
	HD-95 ↓	8.790 (7.994-9.567)	5.898 (5.211-6.630)	5.644 (4.982-6.350)	8.248 (7.328-9.177)		
Multimodal AI	Dice ↑	0.476 (0.434-0.517)	0.609 (0.571-0.648)	0.604 (0.568-0.641)	0.636 (0.603-0.669)		
	IoU ↑	0.331 (0.294-0.369)	0.456 (0.418-0.493)	0.449 (0.414-0.485)	0.482 (0.449-0.516)		
	HD-95 ↓	7.825 (6.487-9.252)	5.355 (4.090-6.778)	4.299 (3.367-5.405)	5.660 (4.734-6.730)		
Center-specific Inference							
		Center A	Center B	Center C			
Multimodal MoME	Dice ↑	0.514 (0.471-0.555)	0.511 (0.471-0.550)	0.558 (0.526-0.590)	0.630 (0.588-0.668)	0.631 (0.591-0.667)	0.648 (0.610-0.683)
	IoU ↑	0.367 (0.327-0.404)	0.361 (0.325-0.397)	0.400 (0.370-0.430)	0.482 (0.441-0.520)	0.480 (0.440-0.516)	0.497 (0.460-0.532)
	HD-95 ↓	6.954 (5.622-8.355)	8.417 (6.880-10.103)	6.716 (5.140-8.495)	3.671 (2.830-4.540)	3.345 (2.657-4.114)	3.970 (3.301-4.684)

Note. **Bold** metric indicates best performance among different few-shot dataset settings, whereas, underline for among entire trials.

values, failing to adequately capture the clinical context for both Center D and Center E. Similarly, the vanilla multimodal model produced a GPR distribution that deviated significantly from the ground truth in both centers. Although the MoME method outperformed the vision-only and vanilla multimodal models, it still showed considerable discrepancies compared to the ground truth GPR distribution. However, when fine-tuning was performed using limited closed center data in

a resource-restricted environment, employing 1-shot, 2-shot, and 3-shot learning, a clear trend of improvement emerged. As the number of fine-tuning samples from the closed centers increased, the GPR distribution became progressively more accurate. This trend was observed across all risk groups in both Center D and Center E, but was particularly pronounced in the high/very high-risk group of Center D. In this group, the GPR distribution closely aligned with the ground truth after 3-shot fine-tuning, demonstrating significant improvement (Supplementary Fig. 4).

Ablation studies in MoME training strategy We conducted further ablation studies by replacing each module within the proposed MoME training strategy to assess the contribution of each component. First, to evaluate the multicenter training method, we designed different strategies to handle diverse data distribution: Text Prompt and Vanilla MoE methods. The Text Prompt method incorporated the center title, such as *Center C*, appended to the input clinical data within the baseline multimodal AI training framework. The Vanilla MoE method used a unified router for all center data, without a center-specific router. The results in Table 3(a) compare these different training methods across three datasets. For both Center A and Center B, the Dice score and IoU were relatively consistent across the three methods, indicating no significant differences among them when applied to the primary training dataset or datasets with similar settings and distributions. In contrast, for Center C, our proposed MoME approach showed a significant improvement in Dice metric by achieving 0.716 compared to the Text Prompt and Vanilla MoE methods with Dice scores of 0.623 and 0.619, respectively. Moreover, MoME training achieved the lowest HD-95 value of 4.132 compared to 5.760 and 5.630 for Text Prompt and Vanilla MoE, respectively, indicating its superior performance with reduced significant contouring errors. These results suggest that incorporating the center-specific router within our proposed MoME structure enhances adaptability during multi-center training, especially when substantial differences in data distribution exist among centers.

We also evaluated the impact of varying the number of experts within the proposed MoME framework (ranging from Top-1 to Top-3), as shown in Table 3(b). Our network consists of a total of 8 expert modules, with the Top-2 method being the baseline. Reducing the number of selected experts to Top-1 led to sparser center-specific training, while increasing it to Top-3 allowed greater overlap of experts across centers. The results showed that using Top-1 experts achieved the best performance for Centers A and B across all metrics, but its performance on Center C was significantly lower with a Dice score of 0.674 compared to the Top-2 strategy with a Dice score of 0.716. Meanwhile, Top-3 experts also demonstrated comparable performance for Centers A and B, but the performance dropped for Center C to below 0.7 in Dice score. These results suggest

that optimal performance in the allocation of experts requires balancing the number of experts in relation to the number of centers to avoid both excessive overlap and excessive sparsity in expert assignments, ensuring the MoME module is effectively adapted to each center-specific strategy.

Table 3: Ablation studies on the network training strategy.

Dataset	Metric	(a) Multicenter Training Method			(b) Top-k Experts for MoME	
		Text Prompt	Vanilla MoE	MoME (Top-2 Experts)	Top-1	Top-3
Center A (n=169 patients)	Dice \uparrow	0.747 (0.720-0.771)	0.744 (0.718-0.768)	0.747 (0.721-0.772)	<u>0.753</u> (0.727-0.778)	0.752 (0.727-0.776)
	IoU \uparrow	0.622 (0.592-0.648)	0.618 (0.589-0.643)	0.623 (0.594-0.648)	<u>0.630</u> (0.602-0.657)	0.627 (0.599-0.653)
	HD-95 \downarrow	3.343 (2.823-3.896)	3.360 (2.870-3.870)	3.407 (2.898-3.956)	<u>2.901</u> (2.539-3.302)	3.108 (2.695-3.537)
Center B (n=117 patients)	Dice \uparrow	0.745 (0.722-0.768)	0.726 (0.699-0.752)	0.750 (0.725-0.773)	<u>0.759</u> (0.730-0.784)	0.731 (0.703-0.757)
	IoU \uparrow	0.608 (0.582-0.634)	0.588 (0.558-0.618)	0.617 (0.588-0.643)	<u>0.630</u> (0.598-0.657)	0.595 (0.564-0.624)
	HD-95 \downarrow	3.181 (2.755-3.647)	3.207 (2.932-3.489)	3.040 (2.773-3.294)	3.084 (2.766-3.426)	3.542 (3.186-3.915)
Center C (n=129 patients)	Dice \uparrow	0.623 (0.587-0.656)	0.619 (0.583-0.655)	0.716 (0.688-0.744)	0.674 (0.627-0.718)	0.660 (0.609-0.709)
	IoU \uparrow	0.479 (0.442-0.513)	0.477 (0.441-0.514)	0.582 (0.553-0.613)	0.536 (0.486-0.583)	0.528 (0.475-0.580)
	HD-95 \downarrow	5.760 (4.770-6.854)	5.630 (4.834-6.449)	4.132 (3.319-5.045)	5.238 (4.263-6.210)	9.362 (7.510-11.279)

Note. **Bold** metric indicates best performance among (a), whereas, underline indicates best performance among (b).

Discussion and Conclusion

Since 2016, following the first FDA approval of a deep learning-based computer-aided diagnostic tool for clinical use ²⁵, research on AI applications in healthcare has grown rapidly, leading to the integration of various AI models into clinical settings ²⁶. Despite these advances, AI in clinical practice still faces persistent challenges, particularly in biases that arise from limited or skewed training data distributions ^{27,28}. Specifically, many healthcare datasets underrepresent minority populations and lack critical demographic data, such as ethnicity and race ²⁹. For instance, a systematic review of cancer image datasets in dermatology revealed that limited population representation hinders these models’ applicability to diverse real-world clinical settings ²⁸. Additionally, in radiology, where data labeling by experts is standard, label inconsistency often arises due to subjective biases of individual clinicians, impacting the reliability of AI models ³⁰. Data distribution shifts further complicate model performance in real-world applications over time, as they can lead to reduced accuracy. Our Mixture of Multicenter Expert (MoME) framework is designed to tackle these challenges by creating tailored center-specific paths that utilize small, diverse samples to ad-

dress inter-institutional variability. This approach aims to enhance model robustness across varied patient demographics and institutional approaches, potentially aligning AI tools more closely with real-world clinical diversity and evolving treatment philosophies.

Radiation oncology is a field where these challenges are particularly pronounced. Despite the existence of international standards such as the National Comprehensive Cancer Network (NCCN) guidelines ²², expert panel consensus, and textbooks based on extensive clinical evidence, inter-clinician variability persists in how treatment protocols are applied. Differences in radiotherapy dose regimens, target structures, and institutional practices are notable. These variations are influenced by factors such as institutional resources, training methodologies, and even cultural factors, which complicate the establishment of a fully standardized approach across regions and clinical settings. To address the challenges of variability in patient characteristics and treatment strategies across different institutions and countries, we proposed the multicenter training strategy that incorporates diverse clinical approaches using MoME modules within a multimodal alignment learning framework. Our center-specific adaptation aims to manage the complexity and heterogeneity of patient populations and treatment protocols. This method allows the model to learn essential knowledge from large-scale datasets for patient treatment planning while simultaneously specializing in each center’s unique patient patterns with just one-shot training across five classes, requiring only 10 additional training samples per center, including a one-shot validation dataset.

The superiority of our multimodal MoME training is demonstrated through both quantitative analyses using traditional metrics like the Dice coefficient and qualitative GPR analysis, which converts center-specific practice patterns into comparable distributions. This analysis showed that the MoME framework effectively aligns with individual center practices. Fig. 3(a) reinforces these findings, showing that center-specific routers enable the model to closely adapt to each center’s treatment patterns, with similar centers exhibiting comparable trends. Our method proves highly adaptable in clinical settings with restricted data sharing but necessary adaptation to new data distributions. As shown in Table 4, MoME enables versatile zero-shot inference scenarios, allowing selection of the most relevant center-specific router using only a few sample test datasets. This addresses long-standing challenges in deploying AI models clinically, demonstrating that the most relevant center-specific inference significantly outperforms the least relevant one and surpasses traditional vision-only and vanilla multimodal inference. Furthermore, one- to three-shot fine-tuning using the selected center-specific router network with MoME outperforms traditional AI training mechanisms for optimizing pre-trained models in deployed clinical settings (Fig. 4). This approach is particularly valuable for real-world applications with limited sample datasets. Experimental re-

sults with varying dataset sizes suggest that our MoME fine-tuning approach efficiently adapts to each institution’s treatment strategies with minimal multicenter data, especially for complex tasks like radiotherapy target volume delineation. This demonstrates the potential for AI-based models to be effectively deployed in clinical scenarios, offering a promising solution for adapting to diverse patient populations and treatment protocols efficiently.

Despite advantages over traditional AI methods, our multicenter training mechanism has limitations. The primary drawback is reliance on limited samples for fine-tuning, potentially restricting model robustness in complex clinical environments. Future research should incorporate larger, more diverse datasets to enhance generalizability. Our method showed relative effectiveness in closed-center fine-tuning, but overall Dice metric performance remained below 0.7, with only marginal improvement compared to multimodal AI. The closed-center setting diverges from MoME’s core rationale of cross-center dataset integration. However, assessment of center A-C synergistic training revealed notable performance gains with joint dataset use. This suggests utilizing publicly accessible datasets could significantly improve closed-center fine-tuning, warranting further exploration. Additionally, evaluation metrics remain constrained. The GPR metric, while useful for visualizing practice pattern differences, is an indirect measure capturing only certain aspects. For instance, in prostate cancer target delineation, the inclusion of seminal vesicles may not be fully reflected in GPR analysis. To address this, future work will incorporate multiple metrics into the MoME model for comprehensive fine-tuning performance evaluation.

Lastly, a crucial next step is addressing inter-clinician variability, expanding beyond institutional differences. This approach aims to account for and mitigate variations in individual clinicians’ strategies and practices, potentially enhancing the model’s adaptability and clinical usability across diverse settings. Implementation will involve an interactive correction system, refining AI-driven outputs through minimal parameter adjustments based on center-specific learning paths. This approach aligns the model with diverse clinical perspectives and supports continual learning reflecting evolving treatment philosophies. Incorporating clinician-specific adaptability could lead to more personalized patient care and improve the model’s generalizability in diverse real-world applications.

In conclusion, our study marks a significant step toward enabling collaboration on multicenter datasets despite challenges associated with large-scale data collection and practical constraints across institutions. The proposed MoME offers an effective method for addressing variability in radiotherapy target delineation practices. Our approach significantly outperformed recent AI train-

ing methods, demonstrating strong generalization to diverse clinical settings and adaptability to distribution shifts. This adaptability further positions the MoME framework as a promising candidate for multicenter collaborations, especially in addressing complex and often debated clinical decision-making tasks by fostering collaborative synergy and aligning with unique institutional strategies.

Methods

Ethic committee approval The hospital data deliberately collected for this study were ethically approved by the Institutional Review Boards (IRB) of the Department of Radiation Oncology at Yonsei Cancer Center, Department of Radiation Oncology at Yongin Severance Hospital, and Department of Radiation Oncology at Gangnam Severance Hospital (IRB numbers 4-2023-0179, 9-2023-0161, and 3-2023-0396, respectively), Department of Radiation Oncology at Mayo Clinic (IRB number 13-005709), and Massachusetts General Hospital (MGH) (IRB number 2022P001512). The requirement for informed consent was waived due to the retrospective nature of the study.

Target volume delineation in prostate cancer radiotherapy In radiation oncology, treatment target volumes are classified as Gross Tumor Volume (GTV), Clinical Target Volume (CTV), and Planning Target Volume (PTV). GTV represents the visible tumor, aligning with the goal of traditional segmentation to delineate observable image regions. CTV, while sometimes derived directly from GTV when a gross tumor is present, typically encompasses areas at risk for microscopic disease. Defining CTV requires consideration of multiple clinical factors, including tumor type, histological findings, cancer stage according to the Tumor, Node, Metastasis (TNM) classification system, and, in specific cases, patient age and performance status. PTV further extends CTV to account for uncertainties in patient setup and positioning.

Radiotherapy for prostate cancer is utilized with definitive, salvage, or palliative intent. Definitive radiotherapy is applied as a curative option when surgery is not feasible due to advanced age, comorbidities, or patient preference. Even in cases where surgery is possible, some patients may choose definitive radiotherapy over radical prostatectomy. For patients who undergo surgery, salvage radiotherapy is administered when rising PSA levels suggest recurrence or when recurrent disease is confirmed. Palliative radiotherapy is often used to manage metastatic disease, such as bone metastases, though target volume delineation in these cases is highly variable due to differing clinical scenarios ²².

In definitive radiotherapy, the target volume typically includes the prostate, seminal vesicles, and areas of suspected extracapsular extension ³¹. For postoperative radiotherapy, the target encompasses the prostate bed and the seminal vesicle bed, with consideration of the surrounding anatomical structures based on the surgical field ³². If lymph node involvement is confirmed, or if the patient falls within the high-risk or very high-risk groups according to NCCN guidelines ²², pelvic nodal irradiation (PNI) is recommended, even in the absence of radiographic evidence of lymph node metastasis. Despite the existence of general principles guiding target volume delineation, there is considerable variability in practice, particularly in the specifics of margin sizes and the inclusion of adjacent structures in cases of suspected locoregional invasion. Intermediate-risk patients with unfavorable factors may also receive PNI depending on institutional protocols, although this is not universally applied.

To reduce variability in target volume delineation, multiple consensus guidelines have been developed for both definitive and postoperative radiotherapy in prostate cancer ^{22,31}. However, significant inter-institutional variability persists, influenced by multifactorial elements including clinician-specific preferences, established institutional protocols, diverse educational paradigms, and region-specific practices that reflect local population demographics and disease characteristics. Complete standardization remains challenging, emphasizing the need for strategies that can adapt to the specific practices of individual institutions while maintaining high standards of care.

Dataset characteristics and clinical context In this study, we utilized datasets from five different centers. Detailed information regarding the number of patients, tumor stage, histopathological grading, PSA levels, surgical status, treatment intent, and imaging acquisition protocols for each center is provided in Supplementary Table 1. Centers A, B, and C are located in South Korea, and while the patient characteristics vary based on the size and location of the centers, they share similar ethnic backgrounds. In contrast, Centers D and E, located in the United States, have a more diverse racial composition compared to the Korean centers (A–C). To address the potential limitations of data sharing between countries, we simulated a closed center environment for Centers D and E. In this scenario, direct data sharing is restricted, and only model weights are transferred. This allowed us to evaluate the feasibility of fine-tuning the MoME model in an in-house setting without exchanging sensitive patient data.

For model training, we utilized the largest dataset from Center A (Yonsei Cancer Center, Seoul, South Korea). A total of 943 primary prostate cancer patients were randomly split, with 774 patients used for training and 169 for internal validation. Center B (Yongin Severance Hospital,

Yongin, South Korea) contributed data from 137 patients. For fine-tuning, 10, 15, or 20 patients were used under different experimental conditions, with the remaining 117 patients reserved for external validation. Similarly, Center C (Gangnam Severance Hospital, Seoul, South Korea) provided data from 149 patients. We used 10, 15, or 20 patients for fine-tuning, while the remaining 129 were used for external validation. For Center D (MGH, Boston, MA, USA), a total of 65 patients were collected, with 10, 15, or 20 patients used for fine-tuning in the closed center setting, and the remaining 45 used for external validation. Finally, Center E (Mayo Clinic, Phoenix, AZ, USA) contributed data from 93 patients, with 10, 15, or 20 patients used for fine-tuning in the closed center environment, and the remaining 73 patients utilized for external validation.

In terms of clinical characteristics, Center A had a higher proportion of locally advanced cases, with a higher tendency towards elevated T stages. In contrast, Centers B and C showed fewer cases with high T stages. This trend was even more pronounced in the U.S. centers (D and E), where T stages were generally even lower than those observed in Centers B and C. Across all institutions, N stage showed minimal variation, with most cases being node-negative, which provided an ideal setting to evaluate institutional policies regarding prophylactic nodal irradiation (PNI). Similar to the T stage trend, the Korean centers (A–C) generally had higher Gleason scores, indicating a greater prevalence of advanced tumors. This was also reflected in the initial PSA values (iPSA), where the Korean institutions reported higher values compared to the U.S. centers. Among them, Center A had the highest iPSA values overall, while the U.S. centers exhibited comparatively lower values. There were also notable differences in the rates of prostatectomy between the Korean and U.S. centers. In the Korean centers, 40% to 80% of patients underwent surgery, whereas approximately more than 70% of patients in the U.S. centers received definitive radiotherapy without surgery. These differences in surgical rates influenced the treatment intent. In the Korean centers, around 50% to over 80% of patients received adjuvant or salvage radiotherapy after surgery, while in the U.S. centers, most patients received definitive radiotherapy without undergoing surgery. Regarding imaging acquisition settings, Centers A and B used similar devices and followed comparable protocols. While Centers C and E employed different settings from A and B, they were closely aligned with each other in their imaging acquisition approaches. In contrast, Center D utilized a distinct combination of devices and protocols, further differentiating it from the other centers. These similarities and differences in imaging acquisition settings, patient demographics (e.g., the similarity between Centers A and B), and clinical practices (e.g., the notable differences between the remaining centers) provided a structured environment to systematically evaluate the effectiveness of MoME in adapting the model to various national and institutional treatment strategies.

To provide relevant clinical context, we extracted key clinical factors essential for prostate cancer radiotherapy from the electronic medical records (EMRs) of each center. These factors were chosen based on their importance for treatment planning and their availability across all institutions. The curated data were then standardized into a formatted clinical dataset, which was used as input for both the multi-modal and MoME models, as shown in Supplementary Table 2.

Multimodal MoME framework The detailed schematic of our proposed network is illustrated in Supplementary Fig. 1. For the image encoder/decoder for each organ extractor and PTV delineation network, we employed the 3D Residual U-Net²⁴. For the large language model (LLM), we utilized the pre-trained Llama3-8B-chat³³ model. Our proposed multimodal MoME is composed of four key steps: (i) prostate segmentation, (ii) interactive multimodal alignment, (iii) center-specific MoME training, (iv) center-specific MoME inference, and (v) closed-center MoME fine-tuning.

(i) Prostate segmentation To guide PTV delineation based on the prostate region, we first use a 3D Residual U-Net²⁴ as the organ extraction module, as illustrated in Supplementary Fig. 1 (a). We trained prostate segmentation module in a supervised manner with the Center A dataset. In the subsequent PTV training phase, we freeze the prostate segmentation module and use the predicted prostate mask $m \in \mathbb{R}^{B \times HWS \times C}$, where B denotes batch size, H , W , S , C correspond to height, width, slice, and channel of prostate mask, as an additional input channel, concatenating it with the input CT scans $x \in \mathbb{R}^{B \times HWS \times C}$ along the channel dimension.

(ii) Interactive multimodal alignment For our multimodal AI training, we adapted a large language model (LLM) to extract clinical data. As illustrated in Supplementary Fig. 1 (b), to efficiently transfer the extensive knowledge of the LLM, we employed text prompt tuning, as previously introduced in our context-aware 3D segmentation network, LLMSeg⁴. By expanding this approach for fine-grained multimodal alignment, we embeds the entire sentence of clinical data through the frozen LLM into L token-wise context embeddings $g \in \mathbb{R}^{L \times D}$, where D is the LLM embedding dimension. To align these context embeddings g with the image embeddings $f_l \in \mathbb{R}^{H_l W_l S_l \times Ch_l}$, where f_l is the output of the l -th layer of the 3D image encoder, with H_l , W_l , and S_l representing the height, width, and slice of the image embeddings, and Ch_l the intermediate channel dimension, we first project g to match the dimensions of each f_l using a layer-wise linear transformation. Then, these linearly projected context embeddings $\bar{g}_l \in \mathbb{R}^{L \times Ch_l}$ are subsequently processed through self-attention and cross-attention mechanisms with the image embeddings f_l within two-way transformer modules of SAM³⁴ structure, resulting in multimodal image embeddings $\bar{f}_l \in \mathbb{R}^{H_l W_l S_l \times Ch_l}$. In contrast to the original LLMSeg, for multicenter training, we further introduced a mixture of

multicenter experts module within the interactive multimodal alignment module.

(iii) Center-specific MoME training We adopt the sparse MoE training mechanisms¹⁸ as the backbone structure of our proposed center-specific, multicenter training framework. The proposed MoME module consists of multiple center-specific router network G^c and shallow multi-layer perceptron neural networks (MLP)-based expert modules. During training, we utilized center flag c , where $c \in \{A, B, C\}$ for representing each Center A, B, and C. Given each data along with this center flag c , the corresponding center-specific router network G^c is selectively activated during both training and inference, and it selects the top- k expert modules E , and outputs of each expert module are then weighted by the output of each center-specific router network.

As illustrated in Supplementary Fig. 1 (c), the multimodal image embeddings \bar{f}_l from each interactive multimodal alignment module are fed to MoME modules. Then, the outputs of the top- k experts with produced center-specific weights W^c are fused, yielding producing center-specific outcomes. Then, the weighted summation of each expert output, which represents the center-specific router path, are combined with \bar{f}_l , which represents the shared path, to yield the final multimodal MoME image embedding \tilde{f}_l , which is computed as follows:

$$\tilde{f}_l = \bar{f}_l + \sum_{i=1}^k G_i^c(\bar{f}_l) \cdot E_i(\bar{f}_l), \quad (1)$$

where $G^c()$ prioritizes each expert’s contribution, and the output \tilde{f}_l from each MoME module has the same shape as \bar{f}_l . We follow the sparse MoE training mechanism¹⁸, where the gating network G computes sparse weight H by adding Gaussian noise, as follows:

$$G(x) = \text{Softmax}(\text{KeepTop-k}(H(x), k)) \quad (2)$$

$$H(x)_i = (x \cdot W)_i + \text{StandardNormal}() \cdot \text{Softplus}(x \cdot W^{\text{noise}})_i \quad (3)$$

$$\text{KeepTop-k}(v, k)_i = \begin{cases} v_i & \text{if } v_i \text{ is in the top } k \text{ elements of } v \\ -\infty & \text{otherwise} \end{cases} \quad (4)$$

where, $\text{Softmax}(\cdot)$ function then normalizes these weights, emphasizing the contribution of the selected experts, $\text{KeepTop-k}(\cdot)$ function selects the k most relevant experts while setting the rest to $-\infty$, and each W and W^{noise} are trainable weight matrices. We set the hyperparameter k as 2.

After the MoME modules, the final mulimodal MoME embeddings \tilde{f}_l for each layer be-

come inputs for the decoder module. The final predicted decoder output \hat{y} is then calculated the combination of the Cross-entropy (CE) loss and the Dice coefficient (Dice) loss by following:

$$\min_{\mathcal{M}} \mathcal{L} = \lambda_{\text{ce}} \mathcal{L}_{\text{ce}}(\hat{y}, y) + \lambda_{\text{dice}} \mathcal{L}_{\text{dice}}(\hat{y}, y), \quad (5)$$

$$\text{where } \mathcal{L}(\hat{y}, y) = -\mathbb{E}_{x \sim P_X} [y_i \log p(\hat{y}_i)], \quad (6)$$

where \mathcal{M} denotes our proposed multimodal MoME network, λ_{ce} and λ_{dice} are hyper-parameters for each CE loss and Dice loss, respectively. $y \in \mathbb{R}^{B \times HWS \times C}$ is the ground-truth PTV mask. $p(\hat{y}_i)$ denotes softmax probability of the i -th pixel within the final predicted output $\hat{y} \in \mathbb{R}^{B \times HWS}$, which is defined as:

$$\hat{y} = \mathcal{M}([x, m]_C, g, c) \quad (7)$$

where x is the input CT scan, m is the predicted prostate mask, $[\cdot]_C$ denotes the channel-wise concatenation operator, g is the context embedding corresponds to the input patient x , and c denotes the center information, where $c \in \{A, B, C\}$.

(iv) Center-specific MoME inference To perform inference using the trained multimodal MoME network, we conducted center-specific inference based on the center flag $c \in \{A, B, C\}$ for the corresponding datasets from Centers A, B, and C, respectively. For external datasets, such as those from Centers D or E, we collected sample test datasets from each center and inferenced them multiple times with every center flag c to activate center-specific router G^c to identify the most relevant router network for zero-shot inference. By comparing the results from each center-specific inference, we selected the best-performing router network using the center flag c .

(v) Closed-center MoME fine-tuning To further fine-tune the multimodal MoME network in an in-house setting, we trained the model with each closed center dataset by utilizing closed center flag $c' \in \{D, E\}$ for representing each Center D and E, based on the pre-trained model weights as the starting point. For fine-tuning the model, we followed the center-specific MoME training approach by utilizing few-shot dataset from each center. For efficiently transferring the pre-trained knowledge, we further froze the image encoder module.

Data pre-processing and model training For data pre-processing, all chest CT images, prostate labels, and PTV labels were resampled to a uniform voxel spacing of $1.0 \times 1.0 \times 3.0 \text{ mm}^3$. Image intensities were truncated between -200 and 250 Hounsfield units (HU) and linearly normalized to a range between 0 and 1.0. During network training, 3D patches of $384 \times 384 \times 128$ pixels

were randomly cropped to include the entire pelvic region, along with the corresponding clinical data, using a batch size of 2. For evaluation, the full 3D CT volumes were processed with a sliding window approach, using the same patch size of $384 \times 384 \times 128$ pixels. Throughout training, the entire large language model (LLM) was frozen, while the image encoder/decoder modules, interactive alignment modules, and text prompts were set as trainable parameters. The loss function combined binary cross-entropy and Dice loss, with equal weights of 1.0. The network was optimized using the AdamW optimizer³⁵, with an initial learning rate of 0.0001, for 100 training epochs. For fine-tuning the network, we optimized only the image decoder, interactive multimodal alignment modules, and text prompts, while keeping the image encoder module and LLM frozen. The learning rate was reduced to 0.00001, and the network parameters were optimized for up to 500 fine-tuning epochs. The network was implemented using the open-source library MONAI². All experiments were conducted using PyTorch³⁶ in Python, leveraging CUDA 11.4 on a single NVIDIA RTX A6000 48GB GPU. For in-house model fine-tuning, we further utilized a single NVIDIA A100 40GB GPU. For multicenter training, we utilized the entire Center A training dataset, combined with 1-shot, 2-shot, and 3-shot samples for each trial from Centers B and C with 1-shot validation samples. The few-shot samples were randomly selected based on Prostate-Specific Antigen (PSA) clusters, where the clusters were categorized as follows: 0 – PSA values below 5.0; 1 – PSA values below 10.0; 2 – PSA values below 20.0; 3 – PSA values below 30.0; and 4 – PSA values above 30.0. For fine-tuning the pre-trained multimodal MoME to adapt to each external center, we utilized 1-shot, 2-shot, and 3-shot samples from each center D or E within their server with 1-shot validation samples.

Evaluation To quantitatively assess PTV delineation performance, we calculated the Dice coefficient (Dice) and Intersection over Union (IoU) for each patient’s PTV delineation result. We further calculated the 95th percentile of the Hausdorff Distance (95-HD)³⁷ to evaluate spatial discrepancies between the ground-truth and predicted contours. For reporting 95-HD, all measured distances in pixel units were adjusted according to the original pixel resolution and reported in centimeters (cm). To further evaluate center-specific PTV delineation strategies, we defined the gross tumor volume (GTV)-to-planning target volume (PTV) ratio (GPR) as the total volume of GTV divided by the total volume of PTV.

Statistics & reproducibility For statistical analysis, we employed the non-parametric bootstrap method to estimate confidence intervals (CIs) for each metric. We performed 1,000 resampling iterations with replacement from the original dataset to generate bootstrap samples. The mean values

²<https://monai.io/>

and 95% CIs were then derived from the relative frequency distributions of these bootstrap samples. Statistical comparisons between groups were conducted using a two-tailed Student's paired t-test. Sample size determination was not based on statistical methods. No data were excluded from the analyses, and the experiments were not randomized. The investigator was not blinded to the allocation during the experiments or outcome assessment.

Data availability

Data availability may be considered by contacting one of the corresponding authors, Kyungsang Kim (kkim24@mgh.harvard.edu), who will assess compliance with these legal provisions. If deemed appropriate, data sharing will proceed following formal inter-institutional collaboration agreements. Initial requests will receive a response within 10 working days. Data usage is restricted to research purposes only, and redistribution is prohibited. No additional documents, such as study protocols or statistical analysis plans, will be provided, and individual patient data will not be directly shared.

Code availability

The Pytorch codes for the proposed Multimodal AI used in this study is available at the following GitHub repository at <https://github.com/tvseg/MoME-RO>

1. E. Huynh, A. Hosny, C. Guthier, D. S. Bitterman, S. F. Petit, D. A. Haas-Kogan, B. Kann, H. J. Aerts, and R. H. Mak, "Artificial intelligence in radiation oncology," *Nature Reviews Clinical Oncology*, vol. 17, no. 12, pp. 771–781, 2020.
2. C. Liu, Z. Liu, J. Holmes, L. Zhang, L. Zhang, Y. Ding, P. Shu, Z. Wu, H. Dai, Y. Li, D. Shen, N. Liu, Q. Li, X. Li, D. Zhu, T. Liu, and W. Liu, "Artificial general intelligence for radiation oncology," 2023.
3. K. Harrison, H. Pullen, C. Welsh, O. Oktay, J. Alvarez-Valle, and R. Jena, "Machine learning for auto-segmentation in radiotherapy planning," *Clinical Oncology*, vol. 34, no. 2, pp. 74–88, 2022.
4. Y. Oh, S. Park, H. K. Byun, Y. Cho, I. J. Lee, J. S. Kim, and J. C. Ye, "Llm-driven multimodal target volume contouring in radiation oncology," *Nature Communications*, vol. 15, no. 1, p. 9186, 2024.

5. P. Rajendran, Y. Chen, L. Qiu, T. Niedermayr, W. Liu, M. Buyyounouski, H. Bagshaw, B. Han, Y. Yang, N. Kovalchuk *et al.*, “Auto-delineation of treatment target volume for radiation therapy using large language model-aided multimodal learning,” *International Journal of Radiation Oncology* Biology* Physics*, 2024.
6. K. Zhang, R. Zhou, E. Adhikarla, Z. Yan, Y. Liu, J. Yu, Z. Liu, X. Chen, B. D. Davison, H. Ren *et al.*, “A generalist vision–language foundation model for diverse biomedical tasks,” *Nature Medicine*, pp. 1–13, 2024.
7. H.-Y. Zhou, S. Adithan, J. N. Acosta, E. J. Topol, and P. Rajpurkar, “A generalist learner for multifaceted medical image interpretation,” *arXiv preprint arXiv:2405.07988*, 2024.
8. K. Singhal, S. Azizi, T. Tu, S. S. Mahdavi, J. Wei, H. W. Chung, N. Scales, A. Tanwani, H. Cole-Lewis, S. Pfohl *et al.*, “Large language models encode clinical knowledge,” *arXiv preprint arXiv:2212.13138*, 2022.
9. I. Fotina, C. Lütgendorf-Caucig, M. Stock, R. Pötter, and D. Georg, “Critical discussion of evaluation parameters for inter-observer variability in target definition for radiation therapy,” *Strahlentherapie und Onkologie*, vol. 188, no. 2, p. 160, 2012.
10. S. K. Vinod, M. Min, M. G. Jameson, and L. C. Holloway, “A review of interventions to reduce inter-observer variability in volume delineation in radiation oncology,” *Journal of medical imaging and radiation oncology*, vol. 60, no. 3, pp. 393–406, 2016.
11. L. Caravatta, G. Macchia, G. C. Mattiucci, A. Sainato, N. L. Cernusco, G. Mantello, M. Di Tommaso, M. Trignani, A. De Paoli, G. Boz *et al.*, “Inter-observer variability of clinical target volume delineation in radiotherapy treatment of pancreatic cancer: a multi-institutional contouring experience,” *Radiation oncology*, vol. 9, pp. 1–9, 2014.
12. M. Barkati, D. Simard, D. Taussky, and G. Delouya, “Magnetic resonance imaging for prostate bed radiotherapy planning: an inter-and intra-observer variability study,” *Journal of Medical Imaging and Radiation Oncology*, vol. 60, no. 2, pp. 255–259, 2016.
13. R. K. Valicenti, J. W. Sweet, W. W. Hauck, R. S. Hudes, T. Lee, A. P. Dicker, F. M. Waterman, P. R. Anne, B. W. Corn, and J. M. Galvin, “Variation of clinical target volume definition in three-dimensional conformal radiation therapy for prostate cancer,” *International Journal of Radiation Oncology* Biology* Physics*, vol. 44, no. 4, pp. 931–935, 1999.
14. F. Shi, W. Hu, J. Wu, M. Han, J. Wang, W. Zhang, Q. Zhou, J. Zhou, Y. Wei, Y. Shao *et al.*, “Deep learning empowered volume delineation of whole-body organs-at-risk for accelerated radiotherapy,” *Nature Communications*, vol. 13, no. 1, p. 6566, 2022.

15. L. Zhang, Z. Liu, L. Zhang, Z. Wu, X. Yu, J. Holmes, H. Feng, H. Dai, X. Li, Q. Li *et al.*, “Segment anything model (sam) for radiation oncology,” *arXiv preprint arXiv:2306.11730*, 2023.
16. K. Chang, N. Balachandar, C. Lam, D. Yi, J. Brown, A. Beers, B. Rosen, D. L. Rubin, and J. Kalpathy-Cramer, “Distributed deep learning networks among institutions for medical imaging,” *Journal of the American Medical Informatics Association*, vol. 25, no. 8, pp. 945–954, 2018.
17. P. Rajpurkar, E. Chen, O. Banerjee, and E. J. Topol, “Ai in health and medicine,” *Nature medicine*, vol. 28, no. 1, pp. 31–38, 2022.
18. N. Shazeer, A. Mirhoseini, K. Maziarz, A. Davis, Q. Le, G. Hinton, and J. Dean, “Outrageously large neural networks: The sparsely-gated mixture-of-experts layer,” *arXiv preprint arXiv:1701.06538*, 2017.
19. G. M. Van de Ven, H. T. Siegelmann, and A. S. Tolias, “Brain-inspired replay for continual learning with artificial neural networks,” *Nature communications*, vol. 11, no. 1, p. 4069, 2020.
20. G. Rypeść, S. Cygert, V. Khan, T. Trzciński, B. Zieliński, and B. Twardowski, “Divide and not forget: Ensemble of selectively trained experts in continual learning,” *arXiv preprint arXiv:2401.10191*, 2024.
21. J. Yu, Y. Zhuge, L. Zhang, P. Hu, D. Wang, H. Lu, and Y. He, “Boosting continual learning of vision-language models via mixture-of-experts adapters,” in *Proceedings of the IEEE/CVF Conference on Computer Vision and Pattern Recognition*, 2024, pp. 23 219–23 230.
22. National Comprehensive Cancer Network, *NCCN Clinical Practice Guidelines in Oncology: Prostate Cancer (Version 4.2024)*, 2024, https://www.nccn.org/professionals/physician_gls/pdf/prostate.pdf.
23. Z. Huemann, J. Hu, and T. Bradshaw, “Contextual net: A multimodal vision-language model for segmentation of pneumothorax,” *arXiv preprint arXiv:2303.01615*, 2023.
24. Ö. Çiçek, A. Abdulkadir, S. S. Lienkamp, T. Brox, and O. Ronneberger, “3d u-net: learning dense volumetric segmentation from sparse annotation,” in *Medical Image Computing and Computer-Assisted Intervention—MICCAI 2016: 19th International Conference, Athens, Greece, October 17-21, 2016, Proceedings, Part II 19*. Springer, 2016, pp. 424–432.
25. S. Benjamens, P. Dhunoo, and B. Meskó, “The state of artificial intelligence-based fda-approved medical devices and algorithms: an online database,” *NPJ digital medicine*, vol. 3, no. 1, p. 118, 2020.
26. D. Shen, G. Wu, and H.-I. Suk, “Deep learning in medical image analysis,” *Annual review of biomedical engineering*, vol. 19, pp. 221–248, 2017.
27. R. Daneshjou, M. P. Smith, M. D. Sun, V. Rotemberg, and J. Zou, “Lack of Transparency and Potential Bias in Artificial Intelligence Data Sets and Algorithms: A Scoping Review,” *JAMA Dermatology*, vol. 157, no. 11, pp. 1362–1369, 11 2021.

28. D. Wen, S. M. Khan, A. J. Xu, H. Ibrahim, L. Smith, J. Caballero, L. Zepeda, C. de Blas Perez, A. K. Denniston, X. Liu, and R. N. Matin, "Characteristics of publicly available skin cancer image datasets: a systematic review," *The Lancet Digital Health*, vol. 4, no. 1, pp. e64–e74, 2022.
29. S. Ganapathi, J. Palmer, J. E. Alderman, M. Calvert, C. Espinoza, J. Gath, M. Ghassemi, K. Heller, F. McKay, A. Karthikesalingam, S. Kuku, M. Mackintosh, S. Manohar, B. A. Mateen, R. Matin, M. McCradden, L. Oakden-Rayner, J. Ordish, R. Pearson, S. R. Pfohl, N. Rostamzadeh, E. Sapey, N. Sebire, V. Sounderajah, C. Summers, D. Treanor, A. K. Denniston, and X. Liu, "Tackling bias in ai health datasets through the standing together initiative," *Nature Medicine*, vol. 28, no. 11, pp. 2232–2233, 2022.
30. A. S. Tejani, T. A. Retson, L. Moy, and T. S. Cook, "Detecting common sources of ai bias: Questions to ask when procuring an ai solution," *Radiology*, vol. 307, no. 3, p. e230580, 2023, PMID: 36943081.
31. C. Salembier, G. Villeirs, B. De Bari, P. Hoskin, B. R. Pieters, M. Van Vulpen, V. Khoo, A. Henry, A. Bossi, G. De Meerleer *et al.*, "Estro acrop consensus guideline on ct-and mri-based target volume delineation for primary radiation therapy of localized prostate cancer," *Radiotherapy and Oncology*, vol. 127, no. 1, pp. 49–61, 2018.
32. A. Dal Pra, P. Dirix, V. Khoo, C. Carrie, C. Cozzarini, V. Fonteyne, P. Ghadjar, A. Gomez-Iturriaga, V. Panebianco, A. Zapatero *et al.*, "Estro acrop guideline on prostate bed delineation for postoperative radiotherapy in prostate cancer," *Clinical and translational radiation oncology*, vol. 41, p. 100638, 2023.
33. AI@Meta, "Llama 3 model card," 2024. [Online]. Available: https://github.com/meta-llama/llama3/blob/main/MODEL_CARD.md
34. A. Kirillov, E. Mintun, N. Ravi, H. Mao, C. Rolland, L. Gustafson, T. Xiao, S. Whitehead, A. C. Berg, W.-Y. Lo *et al.*, "Segment anything," *arXiv preprint arXiv:2304.02643*, 2023.
35. D. Kingma and J. Ba, "Adam: A method for stochastic optimization," in *International Conference on Learning Representations (ICLR)*, San Diego, CA, USA, 2015.
36. A. Paszke, S. Gross, F. Massa, A. Lerer, J. Bradbury, G. Chanan, T. Killeen, Z. Lin, N. Gimelshein, L. Antiga *et al.*, "Pytorch: An imperative style, high-performance deep learning library," *Advances in neural information processing systems*, vol. 32, 2019.
37. W. R. Crum, O. Camara, and D. L. Hill, "Generalized overlap measures for evaluation and validation in medical image analysis," *IEEE transactions on medical imaging*, vol. 25, no. 11, pp. 1451–1461, 2006.

Acknowledgment

This research was supported by the National Research Foundation of Korea (NRF) grant funded by the Korea government (MSIT) (RS-2024-00345854) to Y.O. and (No. 2022R1A2C2008623) to J.S.K., and also supported by Basic Science Research Program through the NRF funded by the Ministry of Education under Grant RS-2023-00242164 to S.P., and by the Hanim Precision Medicine Center of Yonsei University Health System under Grant number (6-2021-0214) to W.S.K.

Author contributions

Y.O. designed the study, extended the code, conducted all experiments, analyzed data, and contributed to manuscript preparation. S.P. conceptualized the study, gathered and labeled the data, analyzed data, and also contributed to manuscript preparation. X.L. designed the study, provided supervision throughout the project, analyzed data, and contributed to manuscript preparation. W.Y., J.P., J.E. and A.C. were responsible for data collection of Massachusetts General Hospital and manuscript preparation. W.S.K., J.W.K., H.K.B., I.J.L., J.C. and C.W.W were responsible for data collection of South Korea and manuscript preparation. P.S., P.W., N.Y., and J.H. were responsible for data collection of Mayo Clinic and manuscript preparation. J.C.Y. provided supervision for conceptualization of the study. Q.L. provided supervision throughout the project, and contributed to manuscript preparation. W.L., W.S.K., J.S.K., and K.K. provided supervision throughout the project, from conception to discussion, and assisted in preparing the manuscript.

Competing interests

There is no competing interest.

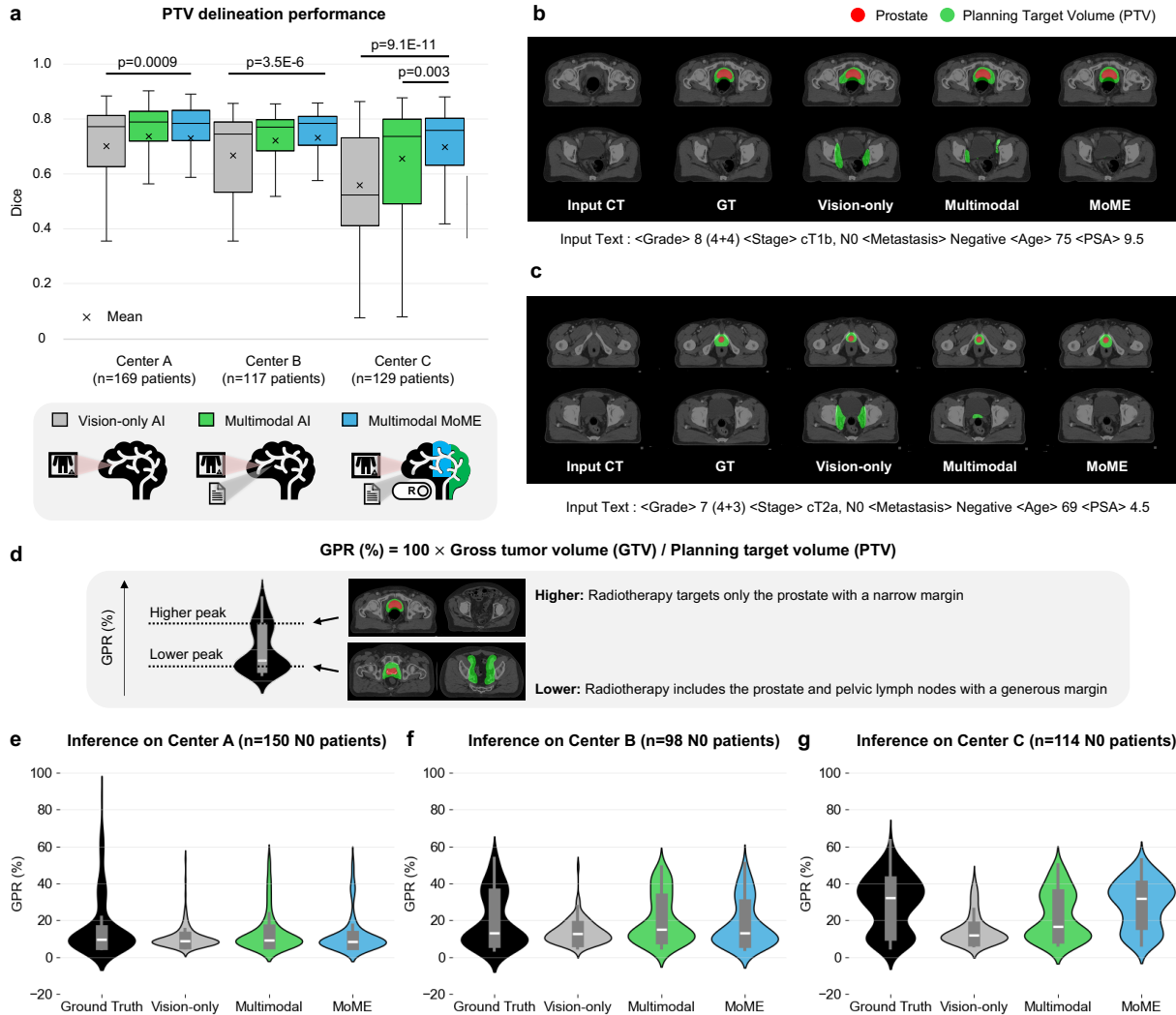


Figure 2: Multicenter AI training comparison on radiotherapy target volume delineation. (a) Quantitative comparison under the multicenter AI training setting. The center line indicates the median, the bounds of the box represent the interquartile range (from the lower quartile to the upper quartile), and the x mark indicates the mean. The p-values indicate the statistically significant superiority of the proposed multimodal MoME to baseline methods. (b) In an intermediate-risk patient case, the institution typically does not perform prophylactic nodal irradiation, yet both vision-only and multimodal AI erroneously included nodes in the delineation. In contrast, the multimodal MoME correctly focused on the prostate, excluding the nodes. (c) In another intermediate-risk, N0 case where none of the models included elective nodal irradiation, the institution generally defines a larger PTV margin around the prostate. The MoME model delineated the target volume with a larger margin, consistent with institutional practice, while both vision-only and multimodal AI applied smaller margins. (d) GTV-to-PTV ratio (GPR) distribution. (e-g) GPR for each Centers A, B, and C patients under different training strategies. The center line indicates the median, and the bounds of the box represent the interquartile range (from the lower quartile to the upper quartile).

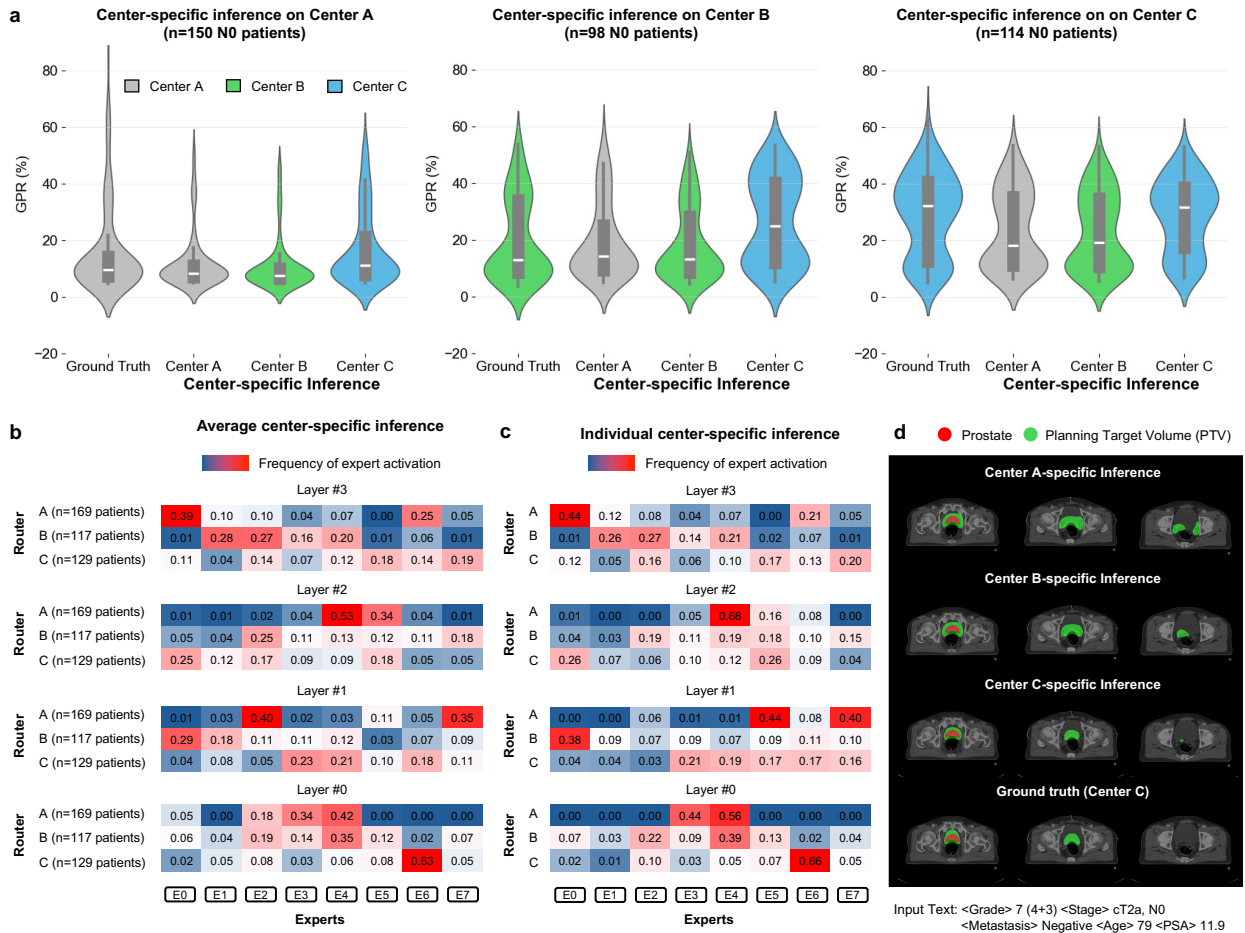


Figure 3: Center-specific inference with the proposed multimodal MoME model. (a) Radiotherapy planning strategy change with different center-specific inference in GTV-to-PTV ratio (GPR) distribution. Given each center dataset as input, the corresponding center inference mostly reflects the planning target strategy. (b) Visualization of average frequency of activated top-k experts for each center dataset with corresponding center-specific router. (c) Visualization of frequency of activated top-k experts for an individual case. For (a-c), the center line indicates the median, and the bounds of the box represent the interquartile range (from the lower quartile to the upper quartile). (d) Qualitative comparison of center-specific inference. Given a CT scan from Center C dataset, activating Center A and B-specific router results in a slightly enlarged PTV margin with prophylactic nodal irradiation, while the correct Center C-specific router aligns closely with the ground truth.

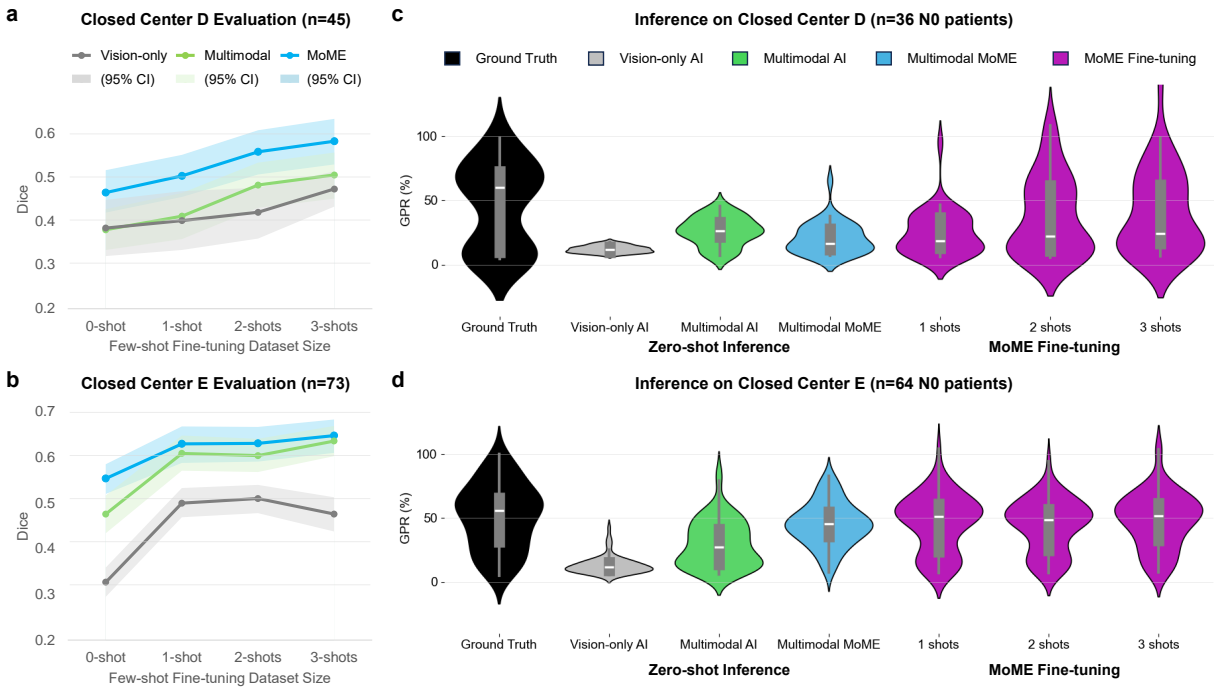


Figure 4: Closed center dataset evaluation. (a) Closed Center D evaluation in Dice metric based on varying few-shot fine-tuning dataset sizes. (b) GTV-to-PTV ratio (GPR) distribution for each method, and MoME fine-tuning result with varying number of few-shot fine-tuning of the closed center D dataset. For (a-b), the Dice metric for each trial is presented as mean values (center lines) with 95th percentile of confidence intervals calculated with the non-parametric bootstrap method (shaded areas). (c) Closed Center E evaluation in Dice metric based on varying few-shot fine-tuning dataset sizes. (d) GPR distribution comparison on closed center E dataset. For (c-d), the center line indicates the median, and the bounds of the box represent the interquartile range (from the lower quartile to the upper quartile).

Supplementary Information

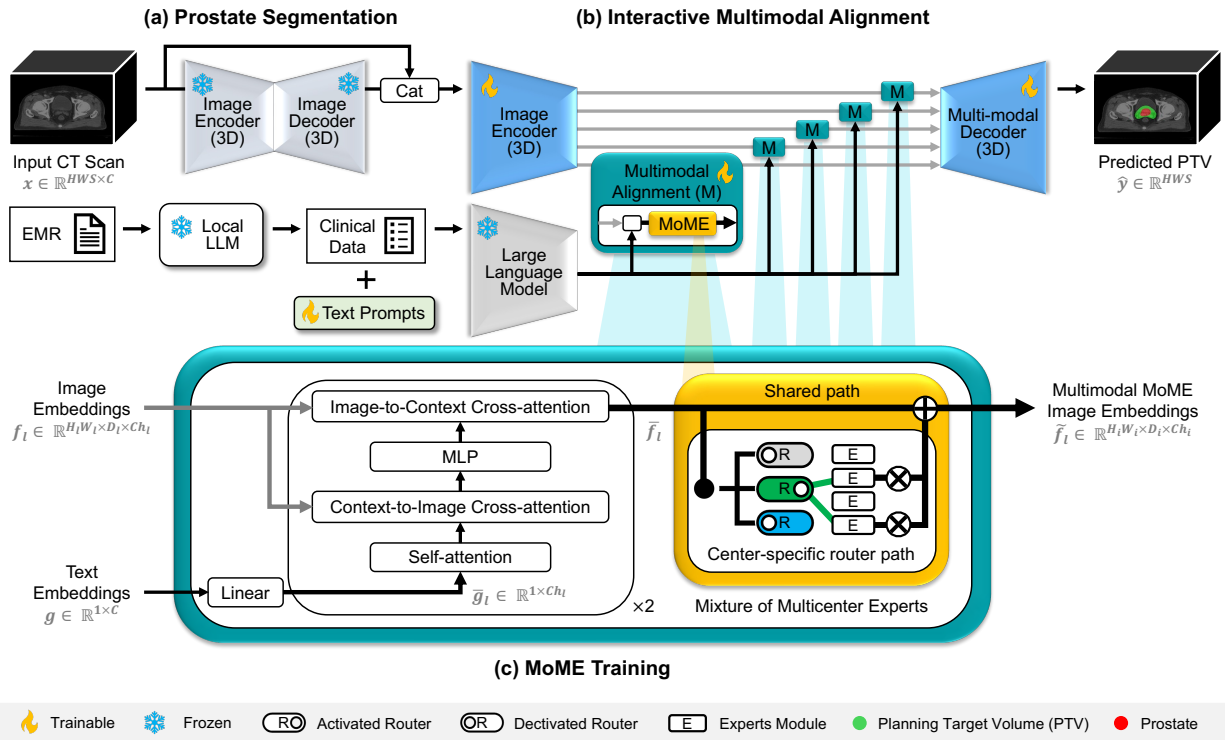
Supplementary Table 1: Details of data partitioning and characteristics for each center.

Center	Center A		Center B	Center C	Center D	Center E
Hospital	Yonsei Cancer Center		Yongin Severance	Gangnam Severance	MGH	MAYO Clinic
Data split	Train (n=774)	Test (n=169)	Train (n=10/15/20 [†]) Test (n=117)	Train (n=10/15/20 [†]) Test (n=129)	Fine-tune (n=10/15/20 [†]) Test (n=45)	Fine-tune (n=10/15/20 [†]) Test (n=73)
T stage						
T1	31 (4.1%)	5 (3.0%)	1 (0.7%)	10 (6.7%)	36 (55.3%)	30 (32.3%)
T2	231 (30.6%)	58 (34.3%)	55 (40.1%)	78 (52.3%)	12 (18.5%)	28 (30.1%)
T3	435 (57.7%)	100 (59.2%)	67 (48.9%)	49 (32.9%)	17 (26.2%)	32 (34.4%)
T4	57 (7.6%)	6 (3.6%)	14 (10.2%)	12 (8.1%)	0 (0%)	3 (3.2%)
N stage						
N0	676 (89.7%)	150 (89.9%)	118 (86.1%)	137 (91.9%)	55 (84.6%)	86 (92.5%)
N1	78 (10.3%)	19 (10.1%)	19 (13.9%)	12 (8.1%)	10 (15.4%)	7 (7.5%)
Gleason score						
5 (2+3)	20 (2.6%)	0 (0%)	0 (0%)	0 (0%)	0 (0%)	0 (0%)
6 (3+3)	42 (5.4%)	6 (3.2%)	17 (12.4%)	17 (11.4%)	6 (9.2%)	9 (9.6%)
7 (3+4, 4+3)	318 (41.1%)	58 (36.0%)	57 (41.6%)	70 (47.0%)	38 (58.5%)	53 (57.0%)
8 (3+5, 4+4, 5+3)	150 (19.4%)	43 (25.4%)	22 (16.1%)	22 (14.8%)	8 (12.3%)	15 (16.1%)
9 (4+5, 5+4)	225 (29.1%)	58 (33.3%)	35 (25.5%)	35 (23.5%)	13 (20.0%)	15 (16.1%)
10 (5+5)	19 (2.5%)	4 (2.1%)	6 (4.4%)	5 (3.4%)	0 (0%)	1 (1.1%)
Initial PSA	39.3 (0.3-3865.0)	39.3 (0.6-682.0)	27.7 (0.9-217.0)	22.2 (2.99-281.67)	12.5 (0.2-126.0)	9.5 (0-156.0)
Prostatectomy						
Yes	511 (66.0%)	129 (76.3%)	55 (40.1%)	70 (47.0%)	9 (13.8%)	30 (32.3%)
No	263 (34.0%)	40 (23.7%)	82 (59.9%)	79 (53.0%)	56 (86.2%)	63 (67.7%)
Therapy purpose						
Definitive	270 (34.9%)	30 (17.8%)	82 (59.9%)	79 (53.0%)	56 (86.2%)	63 (67.7%)
Postoperative	74 (9.6%)	19 (11.2%)	14 (10.2%)	3 (2.0%)	3 (4.6%)	20 (21.5%)
Salvage	431 (55.7%)	120 (71.0%)	41 (29.9%)	67 (45.0%)	6 (9.2%)	10 (10.8%)
CT Scanner						
Manufacturer	Canon	Canon	Canon	SIEMENS	GE	SIEMENS
Model	Aquilion LB	Aquilion LB	Aquilion LB	SOMATOM	Discovery RT	SOMATOM
Scan mode	Helical	Helical	Helical	Helical	Helical	Helical
Filter type	LARGE	LARGE	LARGE	FLAT	BODY	FLAT
kVp	120	120	120	120	140	120
Spatial pixel size (mm)	0.977	0.977	1.367	1.269	0.977	1.269
Slice thickness (mm)	2	2	3	5	1.25	2

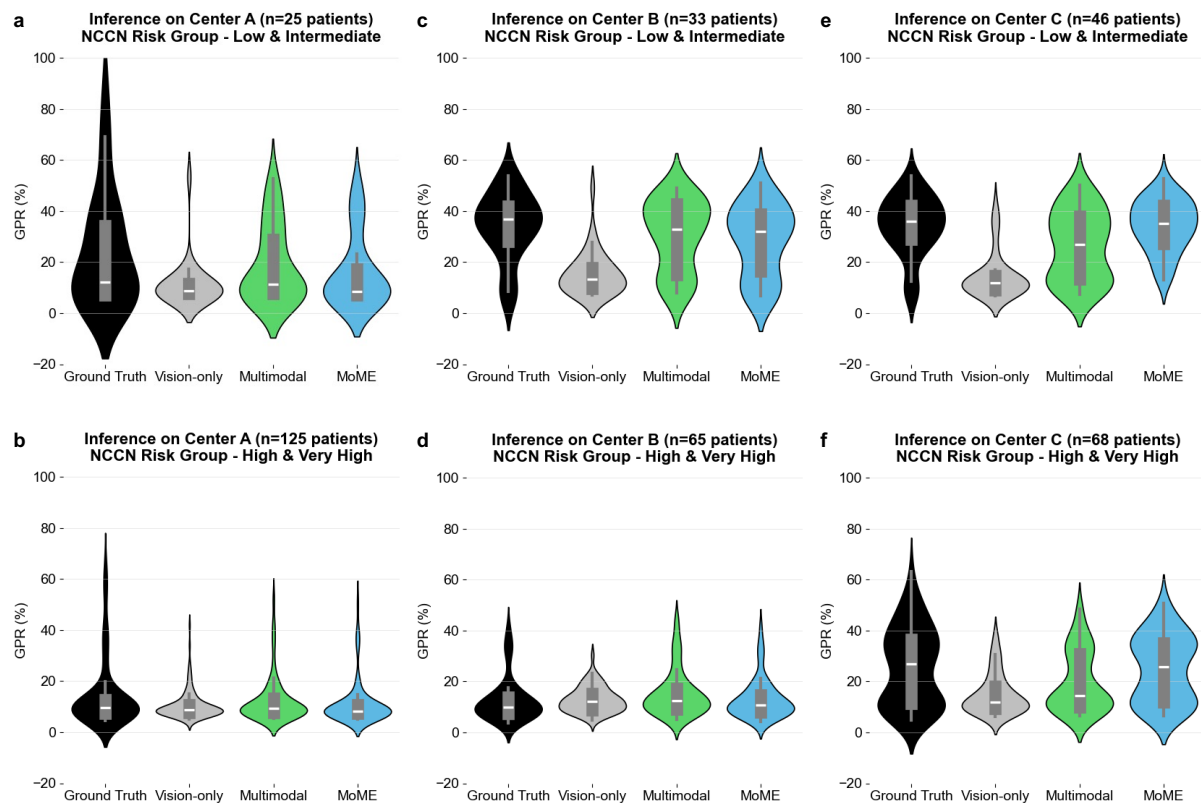
Note. [†] indicates utilized samples for each 1-shot / 2-shots / 3-shots training for each prostate specific antigen (PSA) cluster. PSA clusters (0-4) are categorized as: 0 - PSA values below 5.0, 1 - PSA values below 10.0, 2 - PSA values below 20, 3 - PSA values below 30, and 4 - PSA values above 30.

Supplementary Table 2: Examples of the curated input clinical data from EMR data.

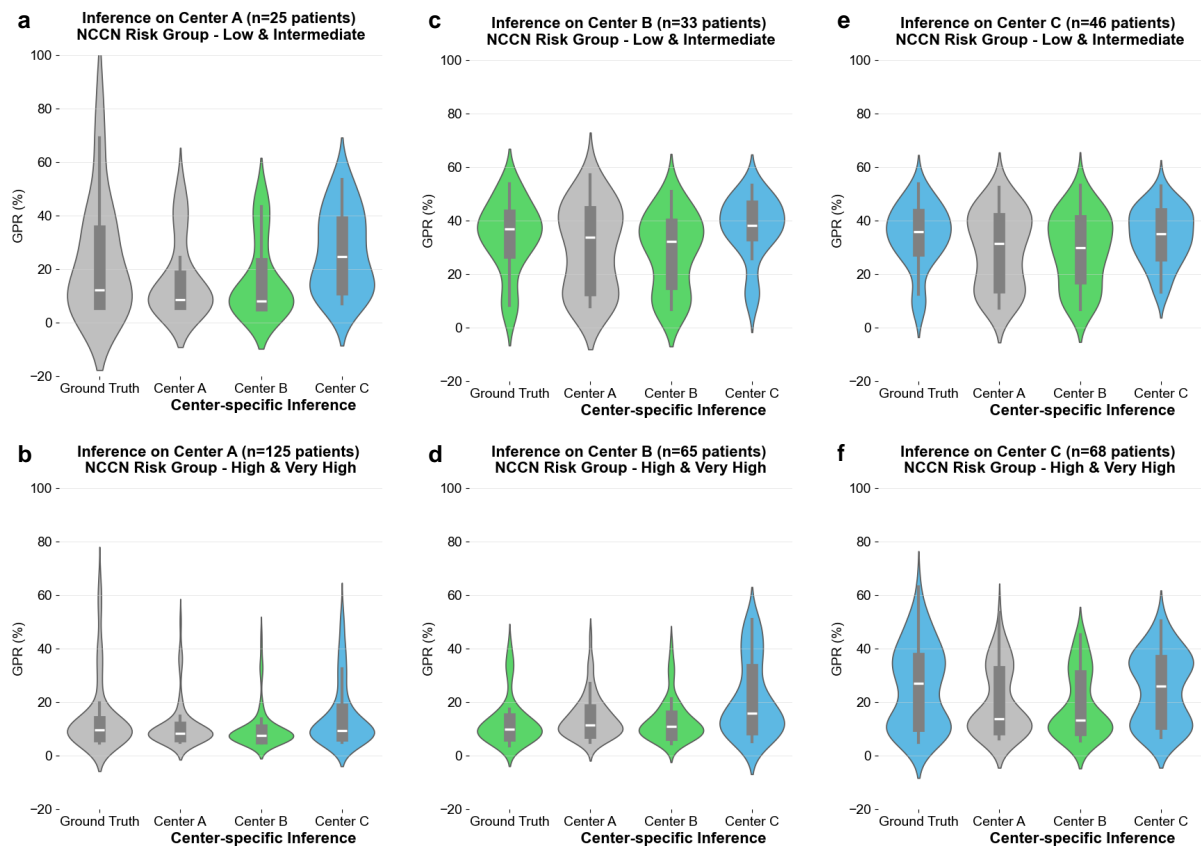
Center	EMR Data (Parsed information)	Input Clinical Data
A,B,C	<p>61-years old patient.</p> <p>#1. Prostate, Adenoca, GS7(4+3), pT3aN0M0, Stage IIIB</p> <ul style="list-style-type: none"> - Tumor location: Both lobes [Index tumor: right, posterior, volume (1.44cc)] - Extraprostatic extension: Present, focal (right posterior, width: 3.0mm, depth: 0.5mm) - Intraglandular tumor volume: V2 (2.64cc) - Lymphovascular invasion: Not identified - Prostatic intraepithelial neoplasia, high grade: Present ... - Vas deferens, right: Free of ca - Vas deferens, left: Free of ca Seminal vesicle, right: Free of ca Seminal vesicle - LN (-), Bone (-) ** iPSA : 8.31 ** Roach score : ECE 52.47 SV 18.31 LN 15.54 s/p Prostate biopsy s/p RALRP #2. Recurrence, prostate PSA elevation @ Prostate MRI No evidence of local recurrence No enlarged LNs on both iliac chain @ PSA 0.72 - 0.43 - 0.08 - 0.01 	<p><Grade> 7 (4+3)</p> <p><Stage> pT3a, N0</p> <p><Metastasis> negative</p> <p><Age> 61</p> <p><PSA> 8.31</p>
D	<p>Tumor markers: Gleason 4+3 = 7</p> <p>Clinical staging: cT1c N0 M0 11.63 IIC</p> <p>Notes: 69 y.o. male with HTN/HLD, orthostatic hypotension, currently on Midodrine</p> <p>...</p> <p>PSA 11.63 prostate cancer, with MRI showing a 73 cc prostate and stable 13 mm index area (PIRADS 3 previously) in the right anterior transition zone at apex and PET CT</p>	<p><Grade> 7 (4+3)</p> <p><Stage> cT1c, N0</p> <p><Metastasis> unknown</p> <p><Age> 69</p> <p><PSA> 11.63</p>
E	<p>diagnosis details: 78-year-old male with a history of rectal cancer status post neoadjuvant chemoradiation.</p> <p>: Gleason 5+4 prostate cancer, PSA 38.4, cT3aN0M0</p> <p>(rectal stenosis unable to do DRE but no T3 per MRI).</p> <p>...</p> <p>Plan PBT 79.2Gy/44fx +18 mo ADT</p>	<p><Grade> 9 (5+4)</p> <p><Stage> cT3a, N0</p> <p><Metastasis> unknown</p> <p><Age> 78</p> <p><PSA> 38.4</p>



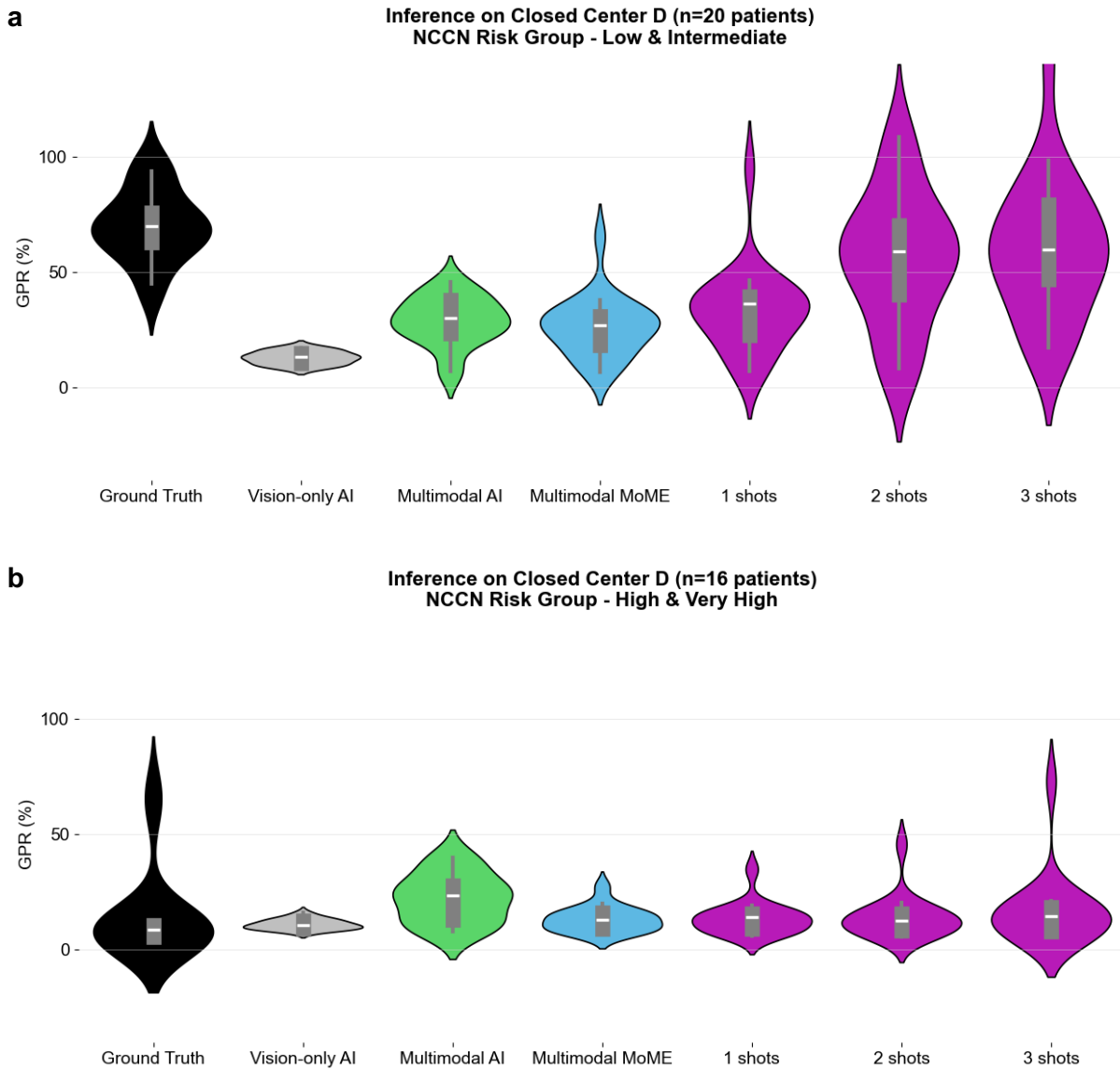
Supplementary Figure 1: Schematic of multimodal mixture of multicenter experts (MoME) network. (a) Prostate segmentation network is pre-trained the resulting prostate mask processed through the frozen prostate segmentation network is added as an additional input to the multimodal MoME network. (b) For our multimodal AI training, we adapted a large language model (LLM) to extract the formatted clinical data curated from electronic medical records (EMRs). This context embeddings are interactively aligned with image embeddings to yield multimodal image embeddings. (c) MoME training splits the input multimodal image embeddings into a shared path and a center-specific router path, which are combined at the end of the MoME module to produce multimodal MoME image embeddings.



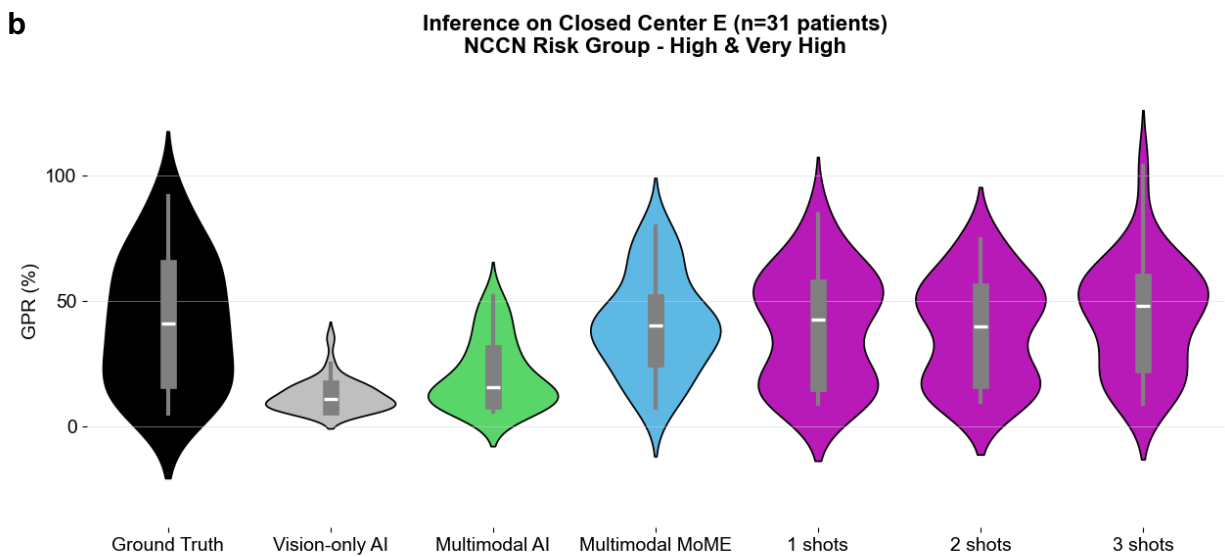
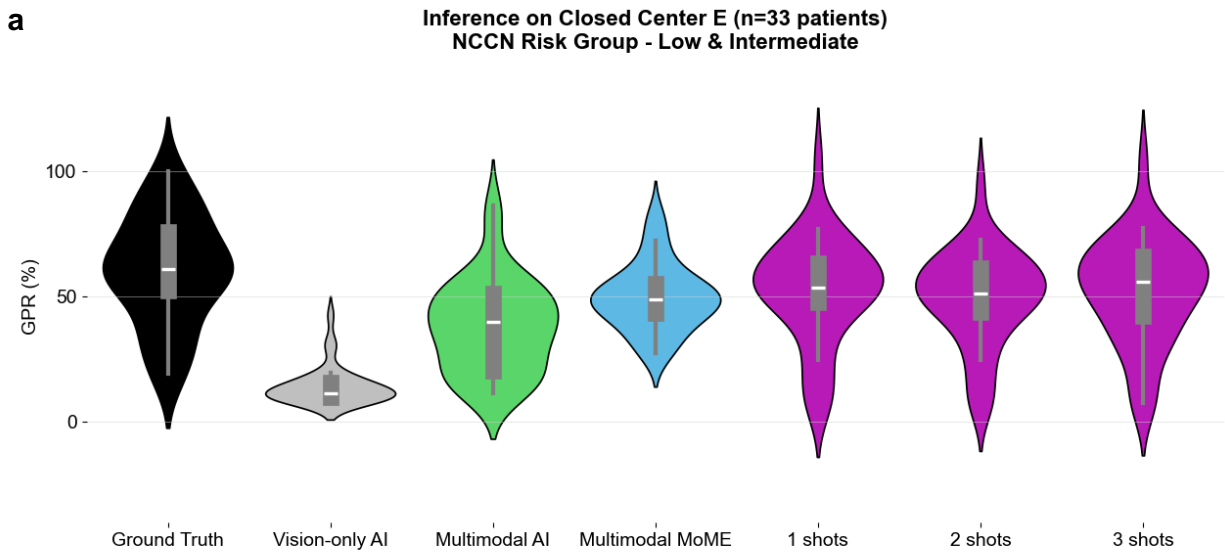
Supplementary Figure 2: Comparison of GTV-to-PTV ratio (GPR) across risk groups for each center by model. The vision-only model consistently demonstrates lower GPR values across all risk groups, showing significant deviation from the ground truth distribution and failing to capture the clinical context. In Centers A and B, the multi-modal and MoME models exhibit similar trends for both (a, c) low/intermediate-risk and (b, d) high/very high-risk groups. However, in Center C, where differences in data acquisition settings, patient distribution, and clinical practice patterns are pronounced, the MoME model more closely aligns with the ground truth GPR distribution compared to the multi-modal model, a trend observed in both (e) low/intermediate-risk and (f) high/very high-risk groups. For (a-f), the center line indicates the median, and the bounds of the box represent the interquartile range (from the lower quartile to the upper quartile).



Supplementary Figure 3: Comparison of GTV-to-PTV ratio (GPR) across risk groups when using each center-specific router. For Center A, both (a) low/intermediate-risk and (b) high/very high-risk groups show the closest alignment with the ground truth GPR distribution when using the Center A expert router, while the Center B expert router produces similar results. In contrast, using the Center C expert router leads to the largest deviation, effectively highlighting the similarities and differences in practice patterns across institutions. For Center B, the (c) low/intermediate-risk and (d) high/very high-risk groups also show consistent alignment with Center B’s original practice when using the Center B expert router, with a similarly close match from the Center A expert router, whereas the Center C expert router again leads to a significant increase in GPR. In Center C, both (e) low/intermediate-risk and (f) high/very high-risk groups display a distinct pattern, with higher GPR values that reflect the center’s less frequent use of PNI and tighter PTV margins. For (a-f), the center line indicates the median, and the bounds of the box represent the interquartile range (from the lower quartile to the upper quartile).



Supplementary Figure 4: Comparison of GTV-to-PTV ratio (GPR) across risk groups for the closed center D. In both (a) low/intermediate-risk and (b) high/very high-risk groups, the MoME model demonstrates a closer alignment with the ground truth distribution compared to the multi-modal as well as the vision only models. This trend becomes more pronounced as the number of examples increases with 1-shot, 2-shot, and 3-shot learning. Notably, in the high-risk group, the GPR distribution produced by the MoME model nearly matches the ground truth with just three-shot fine-tuning. For (a-b), the center line indicates the median, and the bounds of the box represent the interquartile range (from the lower quartile to the upper quartile).



Supplementary Figure 5: Comparison of GTV-to-PTV ratio (GPR) across risk groups for the closed center E. (a) low/intermediate-risk and (b) high/very high-risk groups, the MoME model demonstrates the most similar distribution with the ground truth distribution compared to the multi-modal as well as the vision only models. The distribution gets more similar to the ground truth as the few-shot tuning samples get increased to 3-shot learning, specifically in the low & intermediate group. For (a-b), the center line indicates the median, and the bounds of the box represent the interquartile range (from the lower quartile to the upper quartile).